GEOMETRIC PROPERTIES OF NEURAL MULTIVARIATE REGRESSION: AN EMPIRICAL STUDY

Anonymous authors
Paper under double-blind review

ABSTRACT

Neural multivariate regression underpins a wide range of domains such as control, robotics, and finance, yet the geometry of its learned representations remains poorly characterized. While neural collapse has been shown to benefit generalization in classification, we find that analogous collapse in regression consistently degrades performance. To explain this contrast, we analyze models through the lens of intrinsic dimension. Across control tasks and synthetic datasets, we estimate the intrinsic dimension of last-layer features (ID_H) and compare it with that of the regression targets (ID_Y). Collapsed models exhibit $ID_H < ID_Y$, leading to over-compression and poor generalization, whereas non-collapsed models typically maintain $ID_H > ID_Y$. For the non-collapsed models, performance with respect to ID_H depends on the data quantity and noise levels. From these observations, we identify two regimes—over-compressed and under-compressed—that determine when expanding or reducing feature dimensionality improves performance. Our results provide new geometric insights into neural regression and suggest practical strategies for enhancing generalization.

1 INTRODUCTION

Neural multivariate regression has emerged as a cornerstone of modern machine learning, powering a wide spectrum of applications, including imitation learning, robotic control, financial prediction, and reinforcement learning value approximation. In this work, we empirically investigate the *geometric structure of neural multivariate regression*, with an emphasis on the geometry of last-layer feature vectors.

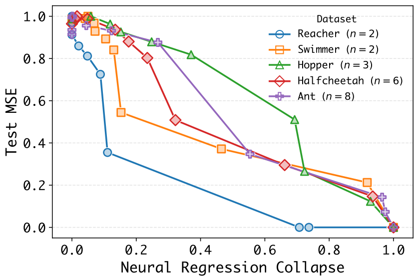

Figure 1: Neural Regression Collapse correlates with high Test MSE. The smaller the NRC value, the closer features lie to the n-dimensional subspace.

Prior efforts have largely framed this problem through the lens of *neural collapse*. In classification, Neural Collapse (NC) describes the emergence of a highly symmetric configuration: last-layer features converge to the vertices of a Simplex Equiangular Tight Frame (ETF), aligned with the classifier weights (Papyan et al., 2020). In regression, by contrast, Neural Regression Collapse (NRC) manifests as the concentration of last-layer features within a linear subspace spanned by the top n principal components of the last-layer feature matrix, where n is the number of target variates. Since n is typically much smaller than the feature dimension, regression collapse implies a major reduction in representational degrees of freedom (Andriopoulos et al., 2024).

In this paper, we first make a key empirical observation: *Collapse, beneficial in classification*[1]*, harms regression models to consistently exhibit degraded generalization as compared to their non-collapsed counterparts*. Figure 1 illustrates this, showing high values of test MSE for models with highly collapsed features (low values of NRC metric) for five robotic locomotion tasks. Existing theoretical and empirical treatments of regression collapse, including the work of Andriopoulos et al. (2024), do not account for this degradation. This raises a central open question: ***Why does neural collapse hinder generalization in multivariate regression, in contrast to its beneficial role in classification?***

---

[1] Appendix B carefully review related work and discuss generalization of neural collapse for classification.

We address this question by employing *intrinsic dimension (ID)*, which quantifies the effective dimensionality of the manifold in which the data lies. As shown in Figure 2 and studied in the paper, intrinsic dimension can capture nonlinearities that the PCA approach of NRC cannot, and thus reveals a more refined geometry of multivariate regression. While intrinsic dimension has been previously studied in the context of neural classification (Ansuini et al., 2019), to the best of our knowledge, this is the first work to analyze neural multivariate regression from this perspective.

2 BACKGROUND AND KEY METRICS

We consider the multivariate regression problem with M training examples $\{(\mathbf{x}_i, \mathbf{y}_i), i = 1, ..., M\}$, where each input $\mathbf{x}_i$ belongs to $\mathbb{R}^D$ and each target vector $\mathbf{y}_i$ belongs to $\mathbb{R}^n$. Considering a deep regression network of the form:

$$f_{\theta,\mathbf{W},\mathbf{b}}(\mathbf{x}) = \mathbf{W}\mathbf{h}_\theta(\mathbf{x}) + \mathbf{b},$$

where $\mathbf{h}_\theta(\cdot) : \mathbb{R}^D \to \mathbb{R}^d$ is the non-linear multi-layer feature extractor, $\mathbf{W} \in \mathbb{R}^{n\times d}$ represents the final linear layer in the model, and $\mathbf{b} \in \mathbb{R}^n$ is the bias vector. The parameters $\theta, \mathbf{W}, \mathbf{b}$ are all trainable. We typically train the DNN using gradient descent to minimize the regularized L2 loss:

$$\min_{\theta,\mathbf{W},\mathbf{b}} \frac{1}{2M}\sum_{i=1}^{M} ||f_{\theta,\mathbf{W},\mathbf{b}}(\mathbf{x}_i) - \mathbf{y}_i||_2^2 + \frac{\lambda_{WD}}{2}(||\theta||_2^2 + ||\mathbf{W}||_F^2),$$

where $||\cdot||_2$ and $||\cdot||_F$ denote the L_2-norm and the Frobenius norm, respectively; and λ_{WD} denotes weight decay parameter.

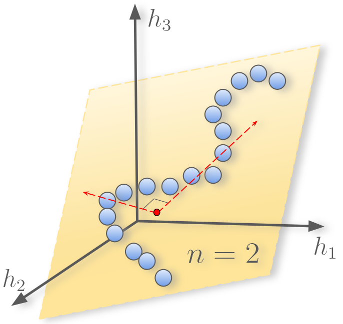

Figure 2: When the target dimension is $n = 2$, the collapsed features (blue points) with intrinsic dimension of 1 can lie close to a subspace (yellow plane) spanned by the first 2 principal components (red arrows) of the features.

Neural Regression Collapse: NRC1 metric Let $\mathbf{h}_i := \mathbf{h}_\theta(\mathbf{x}_i)$ be the feature vector associated with example $\mathbf{x}_i$, $i = 1, \dots, M$. Further let $\widetilde{\mathbf{h}}_i$ be the centered normalized feature vector, that is, $\widetilde{\mathbf{h}}_i := (\mathbf{h}_i - \bar{\mathbf{h}}) \cdot ||\mathbf{h}_i - \bar{\mathbf{h}}||^{-1}$ where $\bar{\mathbf{h}} := M^{-1}\sum_{i=1}^{M}\mathbf{h}_i$. For any $p \times q$ matrix $\mathbf{C}$ and any p-dimensional vector $\mathbf{v}$, let proj$(\mathbf{v}|\mathbf{C})$ denote the projection of $\mathbf{v}$ onto the subspace spanned by the columns of $\mathbf{C}$. Let $\mathbf{H}_{\text{PCA}}$ be the $d \times n$ matrix with the columns consisting of the first n PCs of the feature matrix $\mathbf{H}$. The NRC1 metric is defined as

$$\text{NRC1} := \frac{1}{M}\sum_{i=1}^{M} ||\widetilde{\mathbf{h}}_i - \text{proj}(\widetilde{\mathbf{h}}_i|\mathbf{H}_{\text{PCA}})||_2^2,$$

which measures the extent to which the last-layer features concentrate around their top n principal components. A model is considered collapsed if NRC1 is small, indicating that the features lie almost entirely within an n-dimensional subspace. Non-collapsed models have higher values of NRC1, differing from those of collapsed models by orders of magnitude. Andriopoulos et al. (2024) demonstrated that slightly increased weight decay λ_{WD} quickly leads to model collapse during training. In Appendix G, we empirically demonstrate how weight decay, dropout regularization, and model depth influence NRC1 and ID_H.

Intrinsic Dimension via 2-NN Estimation To uncover the finer geometry of the learned features, beyond what linear methods like PCA reveal, we turn to intrinsic dimension — the minimal number of degrees of freedom needed to describe the data without significant information loss. To estimate the intrinsic dimension, we use the 2-NN estimator, introduced by Facco et al. (2017). For a given point, let r_1 and r_2 denote the distances to its first and second nearest neighbors; define the ratio $\mu := r_2/r_1$. Under the assumption of locally uniform sampling, the cumulative distribution of the ratio follows a Pareto distribution with parameter d: $F(\mu) = 1 - \mu^{-d}$ for $\mu \geq 1$. The intrinsic dimension d is then estimated by linear regression. Details and intuitions are provided in the Appendix C.

3 DATASETS

We perform experiments on robotic locomotion and vision-based datasets described in this section. Full experimental details are included in Appendix A. Moreover, Appendix H examines four more challenging tasks with varying sizes, increased intrinsic dimensions, and visual inputs.

MuJoCo locomotion MuJoCo (Brockman et al., 2016; Towers et al., 2023) is a widely used physics simulator for continuous-control reinforcement learning. Following Andriopoulos et al. (2024), we use Reacher, Swimmer, and Hopper datasets, and additionally include the higher-dimensional Halfcheetah and Ant datasets from the D4RL benchmark (Fu et al., 2020). Each dataset contains expert demonstrations with proprioceptive state inputs ($\mathbf{x}_i$) and corresponding action targets ($\mathbf{y}_i$). States encode joint positions, angles, velocities, and angular velocities, while actions represent joint torques. We subsample the expert data to form low- and high-data regimes of 1,000 and 20,000 samples, respectively.

Vision-based regression We construct two vision-based regression tasks that differ in the amount of task-irrelevant noise present in the targets. In both cases, regression targets are generated by applying a fixed random linear projection to extracted image features. For *MNIST regression*, features are extracted from the penultimate layer of a CNN trained to over 99% accuracy on MNIST, and then projected to 25 dimensions. Because the feature extractor is trained on the same domain, image-feature mismatches are largely suppressed, yielding clean, self-consistent targets. For *CIFAR-10 regression*, features are extracted using a ResNet-18 pretrained on ImageNet and *not* fine-tuned on CIFAR-10, and then projected to 10 dimensions. This domain mismatch causes the projected targets to retain instance-specific, task-irrelevant variation, resulting in noisy targets.

4 INTRINSIC DIMENSION AND GENERALIZATION

By NRC1 definition, this metric does not provide insight into whether the features collapse into lower-dimensional non-linear manifolds. To explore this issue, Figure 3 presents scatter plots for the intrinsic dimension of the last-layer features, denoted ID_H, versus NRC1 for MuJoCo datasets. The intrinsic dimension of the regression targets, ID_Y, is consistently lower than the ambient target dimension n. For highly collapsed models with near-zero NRC1, the intrinsic dimension of last-layer features satisfies $ID_H \lesssim ID_Y < n$ and continues to shrink even as NRC1 saturates at zero, indicating that features lie on increasingly lower-dimensional nonlinear manifolds within an n-dimensional linear subspace. In contrast, non-collapsed models satisfy $ID_H > ID_Y$, and the intrinsic dimension increases monotonically with NRC1, making NRC1 and intrinsic dimension qualitatively interchangeable in this regime. As a result, the following analysis will focus on intrinsic dimension, which reveals a soft threshold at ID_Y separating two NRC regimes and quantifies the degree of collapse (ID_H) across all values of NRC1. Appendix D further analyzes the evolution of intrinsic dimension during training.

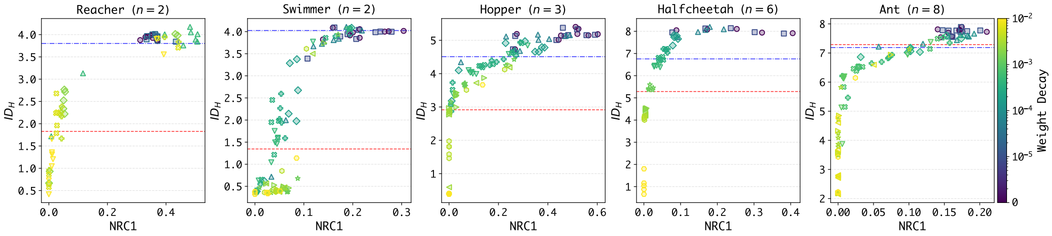

Figure 3: Relationship between NRC1 and intrinsic dimension of the last-layer features ID_H. Dots correspond to models trained with different architectures and weight decay parameters, with the colors denoting the degree of weight decay. The horizontal red dashed line is drawn at ID_Y, and the blue line is drawn at ID_X, the intrinsic dimension of the inputs.

We now turn back to the question raised at the beginning: in Figure 1, why collapsed models suffer increasing generalization error as ID_H (and hence as NRC1) decreases, in contrast to collapse in classification. Figure 4 shows the relationship between ID_H and both training and test MSE for Halfcheetah-1K/20K (1,000 samples/20,000 samples), CIFAR-10, and MNIST datasets. Plots for the remaining datasets are in Appendix F.

Train MSE decreases when $\mathbf{ID_H}$ increases. This trend is evident in the first row of Figure 4. To explain, we note that stronger regularization reduces ID_H from Figure 3 and Figure 11. And Theorems 4.1 and 4.3 in Andriopoulos et al. (2024) also tell that stronger regularization reduces

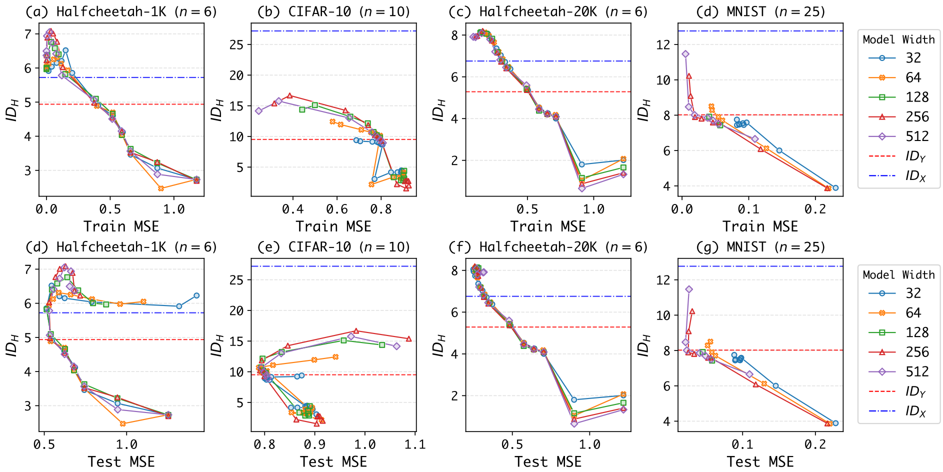

Figure 4: Generalization and Intrinsic Dimension for Halfcheetah, MNIST, and CIFAR-10 datasets.

the dimension of the linear subspace containing the feature manifold. As a result, reducing ID_H effectively squashes features onto more curved, lower-dimensional manifolds. Because the final linear layer $\mathbf{W}$ can only apply affine transformations, it becomes harder to undo this curvature to match the target manifold, explaining the higher training error.

Test MSE with respect to $\mathbf{ID_H}$ behaves differently according to its relationship to $\mathbf{ID_Y}$. The second row of Figure 4 shows fundamental differences between collapsed and non-collapsed models:

- $(ID_H < ID_Y)$: In this regime, the collapsed model's features are confined to a manifold whose intrinsic dimension is lower than that of the targets. This *over-compression* intuitively means the last-layer features lack information essential for reconstructing and generalizing beyond the full target manifold. Theoretical statements in Appendix I show that in this regime, the set of all possible model predictions is a proper subset of the target manifold, thus leading to poor performance on both train and test data for collapsed models.
- $(ID_H \geq ID_Y)$: We distinguish these non-collapsed models between two cases:
  (i) Low-data or noisy-target tasks. In this setting (Figs. 4 (d), (e)), the test MSE exhibits a surprising U-shaped dependence on ID_H, with a minimum near $ID_H \simeq ID_Y$. When training data are scarce or targets are noisy, f_θ learns a feature manifold with intrinsic dimension exceeding that of the true feature manifold, driven by the negative effect of outliers. These extra dimensions capture sample-specific noise, leading to overfitting during training. As regularization is reduced—equivalently, as ID_H increases—this overfitting worsens, resulting in higher test MSE.
  (ii) High-data and low-noise tasks. In this case, test MSE follows the same trend as train MSE, decreasing monotonically with ID_H (Figs. 4 (f),(g)). To explain, we note that with a large amount of training data and low target noise, f_θ can fit the training data closely while maintaining smoothness to avoid overfitting, and consequently, the manifold for $\mathbf{H}_{train}$ is similar to the manifold for $\mathbf{H}_{test}$.

5 CONCLUSION

In this paper, we take the first step towards a systematic geometric analysis of neural multivariate regression through the lens of intrinsic dimension, highlighting a fundamental contrast with classification. We showed that regression collapse corresponds to an over-compressed regime where the feature manifold has a lower intrinsic dimension than the target manifold, leading to poor generalization. In contrast, non-collapsed models typically satisfy $ID_H \geq ID_Y$, with generalization behavior governed by whether the task is low-data/noisy or high-data/low-noise. These results suggest practical criteria for improving generalization by monitoring and adjusting ID_H in applied multivariate regression[2]. In Appendix B and J, we carefully review related work and discuss limitations and future work.

---

[2] In Appendix K, we present an example of evaluating a behaviorally-cloned policy in robotic simulation and illustrate the relationship between its performance and intrinsic dimension.

REFERENCES

Michele Allegra, Elena Facco, Francesco Denti, Alessandro Laio, and Antonietta Mira. Data segmentation based on the local intrinsic dimension. *Scientific reports*, 10(1):16449, 2020.

Laurent Amsaleg, Oussama Chelly, Teddy Furon, Stéphane Girard, Michael E Houle, Ken-ichi Kawarabayashi, and Michael Nett. Estimating local intrinsic dimensionality. In *Proceedings of the 21th ACM SIGKDD International Conference on Knowledge Discovery and Data Mining*, pp. 29–38, 2015.

George Andriopoulos, Zixuan Dong, Li Guo, Zifan Zhao, and Keith W. Ross. The prevalence of neural collapse in neural multivariate regression. In *The Thirty-eighth Annual Conference on Neural Information Processing Systems*, 2024.

Alessio Ansuini, Alessandro Laio, Jakob H Macke, and Davide Zoccolan. Intrinsic dimension of data representations in deep neural networks. *Advances in Neural Information Processing Systems*, 32, 2019.

Sanjeev Arora, Rong Ge, Behnam Neyshabur, and Yi Zhang. Stronger generalization bounds for deep nets via a compression approach. In *International conference on machine learning*, pp. 254–263. PMLR, 2018.

Melih Barsbey, Milad Sefidgaran, Murat A Erdogdu, Gael Richard, and Umut Simsekli. Heavy tails in sgd and compressibility of overparametrized neural networks. *Advances in neural information processing systems*, 34:29364–29378, 2021.

Tolga Birdal, Aaron Lou, Leonidas J Guibas, and Umut Simsekli. Intrinsic dimension, persistent homology and generalization in neural networks. *Advances in neural information processing systems*, 34:6776–6789, 2021.

Léonard Blier and Yann Ollivier. The description length of deep learning models. *Advances in Neural Information Processing Systems*, 31, 2018.

Greg Brockman, Vicki Cheung, Ludwig Pettersson, Jonas Schneider, John Schulman, Jie Tang, and Wojciech Zaremba. Openai gym, 2016.

Johan Samir Obando Ceron, Aaron Courville, and Pablo Samuel Castro. In value-based deep reinforcement learning, a pruned network is a good network. In *Forty-first International Conference on Machine Learning*, 2024a.

Johan Samir Obando Ceron, Ghada Sokar, Timon Willi, Clare Lyle, Jesse Farebrother, Jakob Nicolaus Foerster, Gintare Karolina Dziugaite, Doina Precup, and Pablo Samuel Castro. Mixtures of experts unlock parameter scaling for deep RL. In *Forty-first International Conference on Machine Learning*, 2024b.

Lili Chen, Kevin Lu, Aravind Rajeswaran, Kimin Lee, Aditya Grover, Misha Laskin, Pieter Abbeel, Aravind Srinivas, and Igor Mordatch. Decision transformer: Reinforcement learning via sequence modeling. *Advances in neural information processing systems*, 34:15084–15097, 2021.

Ciprian A Corneanu, Meysam Madadi, Sergio Escalera, and Aleix M Martinez. What does it mean to learn in deep networks? and, how does one detect adversarial attacks? In *Proceedings of the IEEE/CVF Conference on Computer Vision and Pattern Recognition*, pp. 4757–4766, 2019.

Ciprian A Corneanu, Sergio Escalera, and Aleix M Martinez. Computing the testing error without a testing set. In *Proceedings of the IEEE/CVF Conference on Computer Vision and Pattern Recognition*, pp. 2677–2685, 2020.

Misha Denil, Babak Shakibi, Laurent Dinh, Marc'Aurelio Ranzato, and Nando De Freitas. Predicting parameters in deep learning. *Advances in neural information processing systems*, 26, 2013.

Jacob Devlin, Ming-Wei Chang, Kenton Lee, and Kristina Toutanova. Bert: Pre-training of deep bidirectional transformers for language understanding. In *Proceedings of the 2019 conference of the North American chapter of the association for computational linguistics: human language technologies, volume 1 (long and short papers)*, pp. 4171–4186, 2019.

Alexey Dosovitskiy, Lucas Beyer, Alexander Kolesnikov, Dirk Weissenborn, Xiaohua Zhai, Thomas Unterthiner, Mostafa Dehghani, Matthias Minderer, Georg Heigold, Sylvain Gelly, Jakob Uszkoreit, and Neil Houlsby. An image is worth 16x16 words: Transformers for image recognition at scale. In *International Conference on Learning Representations*, 2021.

Scott Emmons, Benjamin Eysenbach, Ilya Kostrikov, and Sergey Levine. Rvs: What is essential for offline RL via supervised learning? In *International Conference on Learning Representations*, 2022.

Elena Facco, Maria d'Errico, Alex Rodriguez, and Alessandro Laio. Estimating the intrinsic dimension of datasets by a minimal neighborhood information. *Scientific reports*, 7(1):12140, 2017.

Cong Fang, Hangfeng He, Qi Long, and Weijie J Su. Exploring deep neural networks via layer-peeled model: Minority collapse in imbalanced training. *Proceedings of the National Academy of Sciences*, 118(43):e2103091118, 2021.

Justin Fu, Aviral Kumar, Ofir Nachum, George Tucker, and Sergey Levine. D4RL: Datasets for deep data-driven reinforcement learning. *arXiv preprint arXiv:2004.07219*, 2020.

Scott Fujimoto, Herke Hoof, and David Meger. Addressing function approximation error in actor-critic methods. In *International conference on machine learning*, pp. 1587–1596. PMLR, 2018.

Tomer Galanti, András György, and Marcus Hutter. On the role of neural collapse in transfer learning. *arXiv preprint arXiv:2112.15121*, 2021.

Quentin Gallouédec, Edward Emanuel Beeching, Clément ROMAC, and Emmanuel Dellandrea. Jack of all trades, master of some, a multi-purpose transformer agent. In *ICML 2024 Workshop: Aligning Reinforcement Learning Experimentalists and Theorists*, 2024.

Peifeng Gao, Qianqian Xu, Yibo Yang, Peisong Wen, Huiyang Shao, Zhiyong Yang, Bernard Ghanem, and Qingming Huang. Towards demystifying the generalization behaviors when neural collapse emerges. *arXiv preprint arXiv:2310.08358*, 2023.

Tianxiang Gao and Vladimir Jojic. Degrees of freedom in deep neural networks. *arXiv preprint arXiv:1603.09260*, 2016.

Li Guo, George Andriopoulos, Zifan Zhao, Shuyang Ling, Zixuan Dong, and Keith Ross. Cross entropy versus label smoothing: A neural collapse perspective. *arXiv preprint arXiv:2402.03979*, 2024.

Tuomas Haarnoja, Aurick Zhou, Pieter Abbeel, and Sergey Levine. Soft actor-critic: Off-policy maximum entropy deep reinforcement learning with a stochastic actor. In *International conference on machine learning*, pp. 1861–1870. Pmlr, 2018.

XY Han, Vardan Papyan, and David L Donoho. Neural collapse under MSE loss: Proximity to and dynamics on the central path. *arXiv preprint arXiv:2106.02073*, 2021.

Takuya Hiraoka, Takahisa Imagawa, Taisei Hashimoto, Takashi Onishi, and Yoshimasa Tsuruoka. Dropout q-functions for doubly efficient reinforcement learning. In *International Conference on Learning Representations*, 2022. URL `https://openreview.net/forum?id=xCVJMsPv3RT`.

Wanli Hong and Shuyang Ling. Neural collapse for unconstrained feature model under cross-entropy loss with imbalanced data. *arXiv preprint arXiv:2309.09725*, 2023.

Daniel Hsu, Ziwei Ji, Matus Telgarsky, and Lan Wang. Generalization bounds via distillation. *arXiv preprint arXiv:2104.05641*, 2021.

Like Hui, Mikhail Belkin, and Preetum Nakkiran. Limitations of neural collapse for understanding generalization in deep learning. *arXiv preprint arXiv:2202.08384*, 2022.

Lucas Janson, William Fithian, and Trevor J Hastie. Effective degrees of freedom: a flawed metaphor. *Biometrika*, 102(2):479–485, 2015.

Ilya Kostrikov, Ashvin Nair, and Sergey Levine. Offline reinforcement learning with implicit q-learning. In *International Conference on Learning Representations*, 2022.

Aviral Kumar, Rishabh Agarwal, Dibya Ghosh, and Sergey Levine. Implicit under-parameterization inhibits data-efficient deep reinforcement learning. In *International Conference on Learning Representations*, 2021.

Aviral Kumar, Rishabh Agarwal, Tengyu Ma, Aaron Courville, George Tucker, and Sergey Levine. DR3: Value-based deep reinforcement learning requires explicit regularization. In *International Conference on Learning Representations*, 2022.

Yann LeCun, John Denker, and Sara Solla. Optimal brain damage. *Advances in neural information processing systems*, 2, 1989.

Hojoon Lee, Dongyoon Hwang, Donghu Kim, Hyunseung Kim, Jun Jet Tai, Kaushik Subramanian, Peter R. Wurman, Jaegul Choo, Peter Stone, and Takuma Seno. Simba: Simplicity bias for scaling up parameters in deep reinforcement learning. In *The Thirteenth International Conference on Learning Representations*, 2025a.

Hojoon Lee, Youngdo Lee, Takuma Seno, Donghu Kim, Peter Stone, and Jaegul Choo. Hyperspherical normalization for scalable deep reinforcement learning. In *Forty-second International Conference on Machine Learning*, 2025b.

Elizaveta Levina and Peter Bickel. Maximum likelihood estimation of intrinsic dimension. *Advances in neural information processing systems*, 17, 2004.

Sergey Levine, Aviral Kumar, George Tucker, and Justin Fu. Offline reinforcement learning: Tutorial, review, and perspectives on open problems. *arXiv preprint arXiv:2005.01643*, 2020.

Chunyuan Li, Heerad Farkhoor, Rosanne Liu, and Jason Yosinski. Measuring the intrinsic dimension of objective landscapes. *arXiv preprint arXiv:1804.08838*, 2018.

Pengyu Li, Xiao Li, Yutong Wang, and Qing Qu. Neural collapse in multi-label learning with pick-all-label loss. *arXiv preprint arXiv:2310.15903*, 2023a.

Qiyang Li, Aviral Kumar, Ilya Kostrikov, and Sergey Levine. Efficient deep reinforcement learning requires regulating overfitting. In *The Eleventh International Conference on Learning Representations*, 2023b.

Tianhong Li and Kaiming He. Back to basics: Let denoising generative models denoise. *arXiv preprint arXiv:2511.13720*, 2025.

Xiao Li, Sheng Liu, Jinxin Zhou, Xinyu Lu, Carlos Fernandez-Granda, Zhihui Zhu, and Qing Qu. Understanding and improving transfer learning of deep models via neural collapse. *arXiv preprint arXiv:2212.12206*, 2022.

Zhuang Liu, Xuanlin Li, Bingyi Kang, and Trevor Darrell. Regularization matters in policy optimization - an empirical study on continuous control. In *International Conference on Learning Representations*, 2021.

Ilya Loshchilov and Frank Hutter. Decoupled weight decay regularization. In *International Conference on Learning Representations*, 2019.

Cong Lu, Philip J. Ball, Tim G. J. Rudner, Jack Parker-Holder, Michael A Osborne, and Yee Whye Teh. Challenges and opportunities in offline reinforcement learning from visual observations. *Transactions on Machine Learning Research*, 2023. ISSN 2835-8856.

Clare Lyle, Mark Rowland, and Will Dabney. Understanding and preventing capacity loss in reinforcement learning. In *International Conference on Learning Representations*, 2022.

Clare Lyle, Zeyu Zheng, Evgenii Nikishin, Bernardo Avila Pires, Razvan Pascanu, and Will Dabney. Understanding plasticity in neural networks. In *International Conference on Machine Learning*, pp. 23190–23211. PMLR, 2023.

Clare Lyle, Zeyu Zheng, Khimya Khetarpal, Hado van Hasselt, Razvan Pascanu, James Martens, and Will Dabney. Disentangling the causes of plasticity loss in neural networks. *arXiv preprint arXiv:2402.18762*, 2024.

Chuang Ma, Tomoyuki Obuchi, and Toshiyuki Tanaka. Neural collapse in cumulative link models for ordinal regression: An analysis with unconstrained feature model. *arXiv preprint arXiv:2506.05801*, 2025.

Xingjun Ma, Bo Li, Yisen Wang, Sarah M Erfani, Sudanthi Wijewickrema, Grant Schoenebeck, Dawn Song, Michael E Houle, and James Bailey. Characterizing adversarial subspaces using local intrinsic dimensionality. *arXiv preprint arXiv:1801.02613*, 2018a.

Xingjun Ma, Yisen Wang, Michael E Houle, Shuo Zhou, Sarah Erfani, Shutao Xia, Sudanthi Wijewickrema, and James Bailey. Dimensionality-driven learning with noisy labels. In *International Conference on Machine Learning*, pp. 3355–3364. PMLR, 2018b.

Dustin G Mixon, Hans Parshall, and Jianzong Pi. Neural collapse with unconstrained features. *arXiv preprint arXiv:2011.11619*, 2020.

Michal Nauman, Michał Bortkiewicz, Piotr Miłoś, Tomasz Trzcinski, Mateusz Ostaszewski, and Marek Cygan. Overestimation, overfitting, and plasticity in actor-critic: the bitter lesson of reinforcement learning. In *Forty-first International Conference on Machine Learning*, 2024a.

Michal Nauman, Mateusz Ostaszewski, Krzysztof Jankowski, Piotr Miłoś, and Marek Cygan. Bigger, regularized, optimistic: scaling for compute and sample efficient continuous control. *Advances in neural information processing systems*, 37:113038–113071, 2024b.

Kei Ota, Devesh K Jha, and Asako Kanezaki. Training larger networks for deep reinforcement learning. *arXiv preprint arXiv:2102.07920*, 2021.

Vardan Papyan, XY Han, and David L Donoho. Prevalence of neural collapse during the terminal phase of deep learning training. *Proceedings of the National Academy of Sciences*, 117(40): 24652–24663, 2020.

Phillip Pope, Chen Zhu, Ahmed Abdelkader, Micah Goldblum, and Tom Goldstein. The intrinsic dimension of images and its impact on learning. *arXiv preprint arXiv:2104.08894*, 2021.

PyTorch Contributors. Pytorch torch.optim.adamw documentation. `https://docs.pytorch.org/docs/stable/generated/torch.optim.AdamW.html`, 2025.

Aravind Rajeswaran, Vikash Kumar, Abhishek Gupta, Giulia Vezzani, John Schulman, Emanuel Todorov, and Sergey Levine. Learning Complex Dexterous Manipulation with Deep Reinforcement Learning and Demonstrations. In *Proceedings of Robotics: Science and Systems (RSS)*, 2018.

Bastian Rieck, Matteo Togninalli, Christian Bock, Michael Moor, Max Horn, Thomas Gumbsch, and Karsten Borgwardt. Neural persistence: A complexity measure for deep neural networks using algebraic topology. *arXiv preprint arXiv:1812.09764*, 2018.

Umut Simsekli, Ozan Sener, George Deligiannidis, and Murat A Erdogdu. Hausdorff dimension, heavy tails, and generalization in neural networks. *Advances in Neural Information Processing Systems*, 33:5138–5151, 2020.

Nitish Srivastava, Geoffrey Hinton, Alex Krizhevsky, Ilya Sutskever, and Ruslan Salakhutdinov. Dropout: A simple way to prevent neural networks from overfitting. *Journal of Machine Learning Research*, 2014.

Peter Súkeník, Christoph H Lampert, and Marco Mondelli. Neural collapse is globally optimal in deep regularized resnets and transformers. *arXiv preprint arXiv:2505.15239*, 2025.

Taiji Suzuki, Hiroshi Abe, Tomoya Murata, Shingo Horiuchi, Kotaro Ito, Tokuma Wachi, So Hirai, Masatoshi Yukishima, and Tomoaki Nishimura. Spectral pruning: Compressing deep neural networks via spectral analysis and its generalization error. *arXiv preprint arXiv:1808.08558*, 2018.

Taiji Suzuki, Hiroshi Abe, and Tomoaki Nishimura. Compression based bound for non-compressed network: unified generalization error analysis of large compressible deep neural network. *arXiv preprint arXiv:1909.11274*, 2019.

Denis Tarasov, Vladislav Kurenkov, Alexander Nikulin, and Sergey Kolesnikov. Revisiting the minimalist approach to offline reinforcement learning. *Advances in Neural Information Processing Systems*, 36:11592–11620, 2023.

Yuval Tassa, Yotam Doron, Alistair Muldal, Tom Erez, Yazhe Li, Diego de Las Casas, David Budden, Abbas Abdolmaleki, Josh Merel, Andrew Lefrancq, Timothy Lillicrap, and Martin Riedmiller. Deepmind control suite, 2018.

Christos Thrampoulidis, Ganesh Ramachandra Kini, Vala Vakilian, and Tina Behnia. Imbalance trouble: Revisiting neural-collapse geometry. *Advances in Neural Information Processing Systems*, 35:27225–27238, 2022.

Tom Tirer and Joan Bruna. Extended unconstrained features model for exploring deep neural collapse. In *International Conference on Machine Learning*, pp. 21478–21505. PMLR, 2022.

Saket Tiwari, Omer Gottesman, and George Konidaris. Geometry of neural reinforcement learning in continuous state and action spaces. In *The Thirteenth International Conference on Learning Representations*, 2025.

Mark Towers, Jordan K. Terry, Ariel Kwiatkowski, John U. Balis, Gianluca de Cola, Tristan Deleu, Manuel Goulão, Andreas Kallinteris, Arjun KG, Markus Krimmel, Rodrigo Perez-Vicente, Andrea Pierré, Sander Schulhoff, Jun Jet Tai, Andrew Tan Jin Shen, and Omar G. Younis. Gymnasium, March 2023. URL `https://zenodo.org/record/8127025`.

Mark Towers, Ariel Kwiatkowski, Jordan Terry, John U Balis, Gianluca De Cola, Tristan Deleu, Manuel Goulão, Andreas Kallinteris, Markus Krimmel, Arjun KG, et al. Gymnasium: A standard interface for reinforcement learning environments. *arXiv preprint arXiv:2407.17032*, 2024.

Kevin Wang, Ishaan Javali, Michał Bortkiewicz, Tomasz Trzcinski, and Benjamin Eysenbach. 1000 layer networks for self-supervised RL: Scaling depth can enable new goal-reaching capabilities. In *The Thirty-ninth Annual Conference on Neural Information Processing Systems*, 2025.

Siwei Wang and Stephanie E Palmer. Towards understanding neural collapse in supervised contrastive learning with the information bottleneck method. *arXiv preprint arXiv:2305.11957*, 2023.

Thomas Wolf, Lysandre Debut, Victor Sanh, Julien Chaumond, Clement Delangue, Anthony Moi, Pierric Cistac, Tim Rault, Rémi Louf, Morgan Funtowicz, Joe Davison, Sam Shleifer, Patrick von Platen, Clara Ma, Yacine Jernite, Julien Plu, Canwen Xu, Teven Le Scao, Sylvain Gugger, Mariama Drame, Quentin Lhoest, and Alexander M. Rush. Transformers: State-of-the-art natural language processing. In *Proceedings of the 2020 Conference on Empirical Methods in Natural Language Processing: System Demonstrations*, pp. 38–45. Association for Computational Linguistics, 2020.

Robert Wu and Vardan Papyan. Linguistic collapse: Neural collapse in (large) language models. *Advances in Neural Information Processing Systems*, 37:137432–137473, 2024.

Guowei Xu, Ruijie Zheng, Yongyuan Liang, Xiyao Wang, Zhecheng Yuan, Tianying Ji, Yu Luo, Xiaoyu Liu, Jiaxin Yuan, Pu Hua, Shuzhen Li, Yanjie Ze, Hal Daumé III, Furong Huang, and Huazhe Xu. Drm: Mastering visual reinforcement learning through dormant ratio minimization. In *The Twelfth International Conference on Learning Representations*, 2024.

Yibo Yang, Shixiang Chen, Xiangtai Li, Liang Xie, Zhouchen Lin, and Dacheng Tao. Inducing neural collapse in imbalanced learning: Do we really need a learnable classifier at the end of deep neural network? *Advances in neural information processing systems*, 35:37991–38002, 2022.

Can Yaras, Peng Wang, Zhihui Zhu, Laura Balzano, and Qing Qu. Neural collapse with normalized features: A geometric analysis over the riemannian manifold. *Advances in neural information processing systems*, 35:11547–11560, 2022.

Denis Yarats, Rob Fergus, Alessandro Lazaric, and Lerrel Pinto. Mastering visual continuous control: Improved data-augmented reinforcement learning. In *International Conference on Learning Representations*, 2022. URL `https://openreview.net/forum?id=_SJ-_yyes8`.

Fan Yin, Jayanth Srinivasa, and Kai-Wei Chang. Characterizing truthfulness in large language model generations with local intrinsic dimension. *arXiv preprint arXiv:2402.18048*, 2024.

Omar G. Younis, Rodrigo Perez-Vicente, John U. Balis, Will Dudley, Alex Davey, and Jordan K Terry. Minari, 2024. URL `https://doi.org/10.5281/zenodo.13767625`.

Jinxin Zhou, Xiao Li, Tianyu Ding, Chong You, Qing Qu, and Zhihui Zhu. On the optimization landscape of neural collapse under MSE loss: Global optimality with unconstrained features. In *International Conference on Machine Learning*, pp. 27179–27202. PMLR, 2022a.

Jinxin Zhou, Chong You, Xiao Li, Kangning Liu, Sheng Liu, Qing Qu, and Zhihui Zhu. Are all losses created equal: A neural collapse perspective. *Advances in Neural Information Processing Systems*, 35:31697–31710, 2022b.

Wei Zhu, Qiang Qiu, Jiaji Huang, Robert Calderbank, Guillermo Sapiro, and Ingrid Daubechies. Ldmnet: Low dimensional manifold regularized neural networks. In *Proceedings of the IEEE conference on computer vision and pattern recognition*, pp. 2743–2751, 2018.

Zhihui Zhu, Tianyu Ding, Jinxin Zhou, Xiao Li, Chong You, Jeremias Sulam, and Qing Qu. A geometric analysis of neural collapse with unconstrained features. *Advances in Neural Information Processing Systems*, 34:29820–29834, 2021.

APPENDIX CONTENTS

A EXPERIMENT DETAILS

Table 1: Overview of datasets employed in the main body.

Dataset	Data Size	Input Type	Input Dim (D)	Input ID (ID_X)	Target Dim (n)	Target ID (ID_Y)
Swimmer	20,000	raw state	8	4.03	2	1.34
Reacher	20,000	raw state	11	3.80	2	1.83
Hopper	20,000	raw state	11	4.51	3	2.91
Halfcheetah	20,000	raw state	17	6.76	6	5.29
Ant	20,000	raw state	111	7.19	8	7.29
MNIST	50,000	Grayscale image	28×28	12.76	25	8.02
CIFAR-10	50,000	RGB image	$32\times 32\times 3$	27.20	10	9.51

A.1 MUJOCO EXPERIMENTS

MuJoCo (Multi-Joint dynamics with Contact) is a physics engine designed for research in robotics, biomechanics, and animation, providing fast and accurate simulations of systems involving complex contact dynamics. It balances physical realism with computational efficiency, enabling reliable modeling of robot–environment interactions (Towers et al., 2024). Environments involved in this work include:

- **Reacher**: A two-jointed robotic arm tasked with moving its tip to a randomly generated target in a 2D plane.
- **Swimmer**: A chain-like robot with three body segments connected by two rotors, aiming to propel itself forward in 2D as quickly as possible.
- **Hopper**: A one-legged, four-part robot that seeks to hop forward at maximum speed in 2D.
- **HalfCheetah**: A planar, bipedal robot with a torso and two legs, each consisting of two joints. It aims to run forward as quickly as possible along a 2D track by coordinating its leg movements.
- **Ant**: A quadrupedal robot with four legs and multiple joints, designed to move in a 3D plane. Its goal is to walk or run forward efficiently, despite the challenge of balancing and coordinating many degrees of freedom. Although Ant's state space has 111 dimensions, 84 of the dimensions related to external contact forces are always zeros in the dataset. Thus, the effective input dimension is 27.

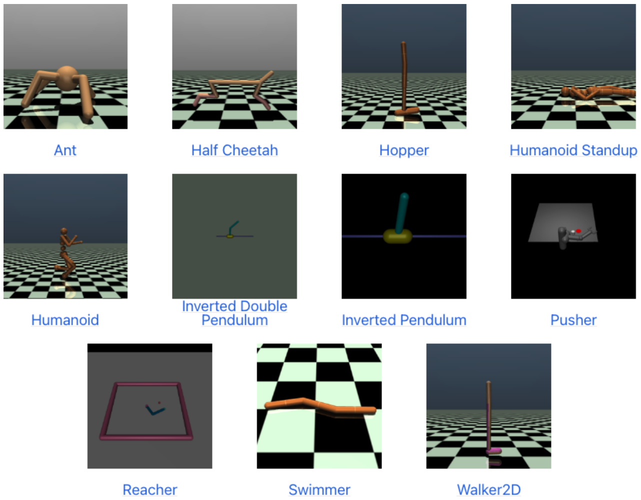

Figure 5: Screenshot of various MuJoCo environments (Towers et al., 2024).

All environments introduce stochasticity by perturbing a fixed initial state with Gaussian noise. Their state spaces combine positions of body and joint with corresponding velocities. Control is achieved by applying joint torques, which serve as the actions. Expert datasets are generated by first training policies through online reinforcement learning (Fu et al., 2020; Gallouédec et al., 2024) until high performance, then executing these policies to produce trajectories of states $\mathbf{x}_i$ and actions $\mathbf{y}_i$. Here, $\mathbf{x}_i$ encodes robot positions, joint angles, velocities, and angular velocities, while $\mathbf{y}_i$ denotes the applied joint torques.

An episode of expert demonstration has a length of 50 for Reacher, and it has a length of 1,000 for all other environments. Thus, by taking 20,000 data points from each expert dataset, the regression model learns from at least 20 complete trajectories to clone the expert's behavior. For evaluation, we retain a subset of the full validation dataset, keeping the number of data points at 20% of the training data size. For small datasets (1K) used in Figures 4, 9 and 10, the test datasets contain 1,000 unseen samples.

There is no absolute threshold for what constitutes "low-data" versus "high-data," as this depends on problem complexity and data structure. In our experiments, we operationally define this distinction using datasets of 1,000 samples versus 20,000 samples—a 20-fold difference that produces qualitatively different generalization behavior. In the low-data regime, the training set provides sparse coverage of the true data manifold, introducing sampling artifacts such as spurious correlations and outlier effects that do not reflect the true underlying distribution. Models trained on such small datasets, particularly without sufficient regularization, tend to memorize these sample-specific patterns rather than learning generalizable structure. In the high-data regime with 20,000 samples, the training set provides denser coverage, the effect of sampling artifacts diminishes, and the empirical distribution more closely approximates the true underlying distribution.

Table 2: All hyperparameter settings involved for experiments on MuJoCo datasets. Each figure employs a subset of possible hyperparameter combinations.

	Hyperparameter	**Value**
Model Architecture	Number of hidden layers	$\{1, 2, 3, 4, 5\}$
	Hidden layer dimension	$\{64, 128, 256, 512, 1024\}$
	Activation function	ReLU
	Number of linear projection layer ($\mathbf{W}$)	1
Training	Epochs	3×10^5 (20K-datasets) 5×10^6 (1K-datasets)
	Batch size	4096 (20K-datasets) 1000 (1K-datasets)
	Optimizer	SGD
	Learning rate	$1 \times 10{-}2$
	Weight decay	$\{0, 1e^{-5}, 1e^{-4}, 3e^{-4}, 5e^{-4}, 7e^{-4}, 1e^{-3}, 3e^{-3}\}$, Reacher $\{0, 1e^{-5}, 1/3/5/7e^{-4}, 1/3/5/7e^{-3}, 1e^{-2}, 3e^{-2}\}$, Otherwise
	Seed	0
	Compute resources	NVIDIA A100 40GB
	Number of CPU compute workers	4
	Requested compute memory	16 GB
	Average training time per model	20 hours

Table 2 summarizes all model hyperparameters and experimental settings for MuJoCo datasets. A subset of possible hyperparameter combinations is used for each figure:

- Figure 1 plots the min-max normalized Test MSE as a function of the min-max normalized NRC1 values for the model architecture 3-256 (3 hidden layers and 256 hidden units) and all possible weight decay values.
- Figure 3 establishes the relationship between NRC1 and ID_H. Each subplot includes all weight decays listed in Table 2. And each weight decay is combined with 9 model architectures in {3-64, 3-128, 3-256, 3-512, 3-1024, 1-256, 2-256, 4-256, 5-256}.
- Figs. 4, 9 and 10 empirically reveal how generalization ability is affected by ID_H. We focus on a single model depth of 3, and vary the model width among $\{64, 128, 256, 512, 1024\}$. For each model architecture, we evaluate all possible weight decay values listed in Table 2.
- Figure 6 depict how intrinsic dimension evolves for each network layer. The model architecture is fixed at 3-256 and the title of each subplot annotates the weight decay value.

- Figure 7 and 8 follow the same experimental setup as Figs. 4, 9 and 10, but emphasize on the comparison between ID_H and ID_P.
- Figure 11 record NRC1 values along the training process. The model architecture is fixed to 3-256 for all datasets. And we show 10 weight decay values in $\{0, 0.0001, 0.0003, 0.0005, 0.0007, 0.001, 0.003, 0.005, 0.007, 0.01\}$.

A.2 MNIST/CIFAR10 EXPERIMENTS

The regression models for both the MNIST and CIFAR-10 tasks were trained across a spectrum of hyperparameters to thoroughly investigate the effects of architecture and regularization on the learned representations. The specific settings for model architecture, optimizer, and other training parameters are detailed in Table 4.

Table 3: All hyperparameter settings involved for experiments on MNIST and CIFAR-10 datasets.

	Hyperparameter	**Value**
Model Architecture	Number of hidden layers	3
	Hidden layer dimension	$\{32, 64, 128, 256, 512\}$
	Activation function	ReLU
Training	Epochs	200
	Batch size	64
	Optimizer	Adam
	Learning rate	$\{1 \times 10^{-3}, 5 \times 10^{-3}\}$
	Weight decay (MNIST)	$\{0, 10^{-5}, 10^{-4}, 3 \times 10^{-4}, 5 \times 10^{-4}, 7 \times 10^{-4}, 10^{-3}, 3 \times 10^{-3}, 7 \times 10^{-3}\}$
	Weight decay (CIFAR-10)	$\{0, 10^{-5}, 10^{-4}, 3 \times 10^{-4}, 5 \times 10^{-4}, 7 \times 10^{-4}, 10^{-3}\}$
	Seed	0
	Compute resources	NVIDIA A100 80GB
	Average training time per model	2 hours

We define noisy-target tasks as tasks where the regression targets contain information that causes models to learn patterns that do not generalize to unseen data. The term "noise" here does not refer to random measurement error or label corruption, but rather to information that varies between semantically similar examples due to instance-specific characteristics rather than reflecting the true underlying function.

The synthetic MNIST regression task represents a low-noise setting. The feature extractor is a CNN trained specifically on MNIST until achieving over 99% classification accuracy, creating a self-consistent target-generation pipeline. During training, the CNN learns to discard instance-specific variations (such as stroke thickness, slight rotations, or pixel-level noise) that are irrelevant for predicting the target label, retaining only the semantically meaningful information. As a result, the mapping from MNIST images to projected features is smooth and well-aligned with the data domain, enabling models to generalize effectively (Figs. 4 (d),(g)).

In contrast, the synthetic CIFAR-10 regression task is a noisy-target setting due to domain mismatch. CIFAR-10 images are processed through a ResNet-18 pretrained on ImageNet to extract features, which are then projected to 10-dimensional targets. The ImageNet encoder captures fine-grained visual details—texture patterns, color distributions, edge structures—optimized for ImageNet's 1,000 classes. When applied to CIFAR-10's 32×32 images, these features encode not only semantic content but also instance-specific characteristics: two images of cars may differ in color, lighting, rendering artifacts, or background elements, all of which significantly influence the extracted features. Models can fit these instance-specific components during training, achieving low training error. However, at test time, new images from the same semantic classes exhibit different instance-specific details. The learned mappings for these non-generalizable components do not transfer, resulting in poor generalization. This is evident in Figs. 4 (b),(e), where models achieve low training MSE but high test MSE, characteristic of overfitting to target noise.

B RELATED WORK

NC under varied settings on classification. The phenomenon of neural collapse was first empirically observed by Papyan et al. (2020), who demonstrated its emergence during TPT in deep neural network models for classification tasks. Building on this empirical finding, researchers have developed theoretical frameworks to analyze NC, such as the Unconstrained Feature Model (UFM) (Mixon et al., 2020) and the layer-peeled model (Fang et al., 2021). Using these models, numerous studies have demonstrated that NC provably occurs under diverse conditions (Han et al., 2021; Tirer & Bruna, 2022; Yaras et al., 2022; Zhou et al., 2022a;b; Zhu et al., 2021) and using various loss functions such as label smoothing (Guo et al., 2024). See also (Hong & Ling, 2023; Thrampoulidis et al., 2022; Yang et al., 2022).

NC beyond single-label classification. Recent research has extended the principles of NC beyond its original single-label classification setting. Li et al. (2023a) demonstrated that in multi-label classification, embeddings reside within the linear span of their label means. Andriopoulos et al. (2024) generalized NC to neural multivariate regression, formalizing it as Neural Regression Collapse (NRC). Ma et al. (2025) showed that NC emerges in deep ordinal regression, analyzing it through the UFM framework. In large language models, Wu & Papyan (2024) identified a "linguistic collapse". Súkeník et al. (2025) proved that NC represents the globally optimal configuration in modern deep regularized architectures, including ResNets and transformers.

Intrinsic dimension in deep neural networks. Several works investigate the intrinsic dimension of data manifolds and representations in deep neural networks (Denil et al., 2013; LeCun et al., 1989). Classical methods estimate intrinsic dimension from local neighborhoods (Allegra et al., 2020; Amsaleg et al., 2015; Facco et al., 2017; Levina & Bickel, 2004), which have been extended to neural settings. Ma et al. (2018a) show that local intrinsic dimension (LID) can distinguish adversarial from natural image data. More recently, Yin et al. (2024) focused on per-sample LID to identify when LLMs produce untruthful outputs.

A parallel line of research uses tools from topological data analysis to study neural networks. Some works analyze the trained network by constructing topological invariants from layer weights, such as Neural Persistence (Rieck et al., 2018), which can distinguish between models that overfit or generalize well. Others analyze the underlying graph structure of networks (Corneanu et al., 2019; 2020). While often empirical, these approaches provide a novel perspective on network properties. More recent work (Birdal et al., 2021) has begun to place these topological methods on a firmer theoretical foundation using statistical persistent homology.

Beyond empirical estimations, intrinsic dimension has been studied as a measure of model complexity. Recent approaches analyze the degrees of freedom in parameter space (Gao & Jojic, 2016; Janson et al., 2015), compressibility via pruning (Blier & Ollivier, 2018), and intrinsic dimension (Ansuini et al., 2019; Li et al., 2018; Ma et al., 2018b; Pope et al., 2021). Compression-based generalization bounds (Arora et al., 2018; Barsbey et al., 2021; Hsu et al., 2021; Suzuki et al., 2018; 2019) have shown that networks that can be represented in a lower-dimensional space exhibit lower generalization error. See also Simsekli et al. (2020); Birdal et al. (2021); Zhu et al. (2018).

Comparison between Regression and Classification Previous work on manifold learning for neural classification has demonstrated that the intrinsic dimension of the last hidden layer is negatively correlated with generalization ability. In particular, models achieving lower intrinsic dimension in the penultimate layer were found to exhibit superior test accuracy, with the lowest intrinsic dimension-model attaining the highest top-5 accuracy, see Section 3.2 and Figure 4 in Ansuini et al. (2019). Additionally, Papyan et al. (2020) connect neural collapse to robust decision boundaries, Galanti et al. (2021) demonstrate that collapse patterns improve few-shot and transfer learning, and Li et al. (2022) show the degree of collapse in downstream representations strongly predicts transfer accuracy. Complementing these empirical results, there are also theoretical results showing the benefits of neural collapse for classification (Gao et al., 2023; Wang & Palmer, 2023; Hui et al., 2022).

In regression, however, our findings indicate a more nuanced picture. We demonstrated the existence of a "soft" threshold at ID_Y, which delineates distinct generalization regimes. In the under-compressed regime with low-data tasks and high-noise tasks, reducing ID_H improves generalization, consistent with the monotonic complexity-performance paradigm observed in classification. However, in the over-compressed regime and in the under-compressed regime with high-data tasks and low-noise tasks, the opposite holds: increasing ID_H improves generalization, a phenomenon absent in classification tasks. Thus, in regression, generalization performance depends non-monotonically on the relationship between the learned feature manifold and the intrinsic dimension of the targets.

C INTRINSIC DIMENSION AND THE 2-NN ALGORITHM

The intrinsic dimension (ID) of a dataset is the minimum number of coordinates needed to represent the data faithfully. If data points lie on or near a d-dimensional manifold $\mathcal{M}$ embedded in $\mathbb{R}^D$ with $d \ll D$, then d is the intrinsic dimension. For example, a circle in 3D space has $d = 1$ and a sphere surface in 10D has $d = 2$.

A critical distinction exists between PCA dimensionality and intrinsic dimension. Consider a 1D spiral embedded in $\mathbb{R}^{10}$ parameterized by t. The spiral winds through space with substantial variance across all 10 axes, requiring multiple PCA components to capture the signal. Yet, the intrinsic dimension is exactly $d = 1$, because specifying a single scalar value, such as the arc length from the origin, is sufficient to uniquely locate any point on the curve. This illustrates that curved or folded manifolds can require many linear directions to approximate while having low intrinsic dimension. Figure 2 demonstrates this for neural regression: collapsed features lie near a 2D linear subspace (yellow plane) yet occupy a nonlinear 1D manifold within it.

We estimate ID using the 2-NN estimator (Facco et al., 2017), which exploits a fundamental geometric property: in a d-dimensional space, the probability of finding neighbors within a given distance scales with dimension d. The key insight is to consider not absolute distances, but the ratio $\mu = r_2/r_1 \geq 1$ of the second to first nearest-neighbor distances. Remarkably, under the assumption of locally uniform density (density approximately constant within the range of the second neighbor), this ratio has a distribution that depends only on the intrinsic dimension d, with the local density completely canceling out. Specifically, the cumulative distribution function of μ is

$$F(\mu) = 1 - \mu^{-d}, \quad \mu \geq 1$$

This property makes the estimator robust to density variations, since we never need to estimate the density itself. Taking logarithms yields the linear relationship

$$\log(1 - F(\mu)) = -d \log \mu$$

The 2-NN algorithm estimates d by computing μ_i for each point, constructing the empirical CDF F_{emp}, and performing linear regression on the transformed coordinates $\{(\log \mu_i, -\log(1 - F_{\text{emp}}(\mu_i)))\}$. The requirement of local uniformity only within the second-neighbor distance is much weaker than global uniformity, making the estimator practical for real datasets with varying density and curvature.

Algorithm 1: 2-NN Intrinsic Dimension Estimation

```
Input: Dataset $\mathcal{X} = \{\mathbf{x}_i\}_{i=1}^{M}$.
Output: Estimated intrinsic dimension $\hat{d}$.
for $i \leftarrow 1$ to $M$ do
    Compute Euclidean distances to the first and second nearest neighbors, $r_1(\mathbf{x}_i)$ and $r_2(\mathbf{x}_i)$;
    Compute ratio $\mu_i \leftarrow r_2(\mathbf{x}_i)/r_1(\mathbf{x}_i)$;
Sort the ratios such that $\mu_{\sigma(1)} \leq \mu_{\sigma(2)} \leq \cdots \leq \mu_{\sigma(M)}$;
for $i \leftarrow 1$ to $M$ do
    Assign empirical CDF value $F_{emp}(\mu_{\sigma(i)}) \leftarrow \frac{i}{M}$;
Construct the coordinate set for regression:
    $\mathcal{S} \leftarrow \left\{ \left( \log \mu_{\sigma(i)},\ -\log\left(1 - F_{emp}(\mu_{\sigma(i)})\right) \right) \right\}_{i=1}^{M-1}$
Fit a line through the origin to $\mathcal{S}$ using least squares;
return Slope of the fitted line ($\hat{d}$);
```

D EVOLUTION OF INTRINSIC DIMENSION DURING TRAINING

To further understand the behavior of collapsed models and their counterparts, we track the evolution of the intrinsic dimension throughout training and provide insights. Figure 6 provides illustrative examples for a collapsed and a non-collapsed model:

- For both the collapsed and non-collapsed models, the intrinsic dimension of the last-layer features invariably decreases monotonically until convergence.
- For the collapsed model, the deeper the layer in the network, the lower the intrinsic dimension at the end of training. ReLU activations cause a mild reduction in intrinsic dimension in comparison with the reduction in intrinsic dimension between consecutive layers (ignoring ReLU). Notably, the final intrinsic dimension of the output layer, which gives the actual vector-valued predictions, can be significantly lower than ID_H.
- For non-collapsed models, we usually see — but not always — ID_H decrease monotonically as we move from shallow to deep layers. Furthermore, we observe that during training, the intrinsic dimension of the output layer hugs the intrinsic dimension of the targets. Thus, tracking the intrinsic dimension of the output layer provides yet another criterion for discriminating between collapsed and non-collapsed models; see Appendix E.

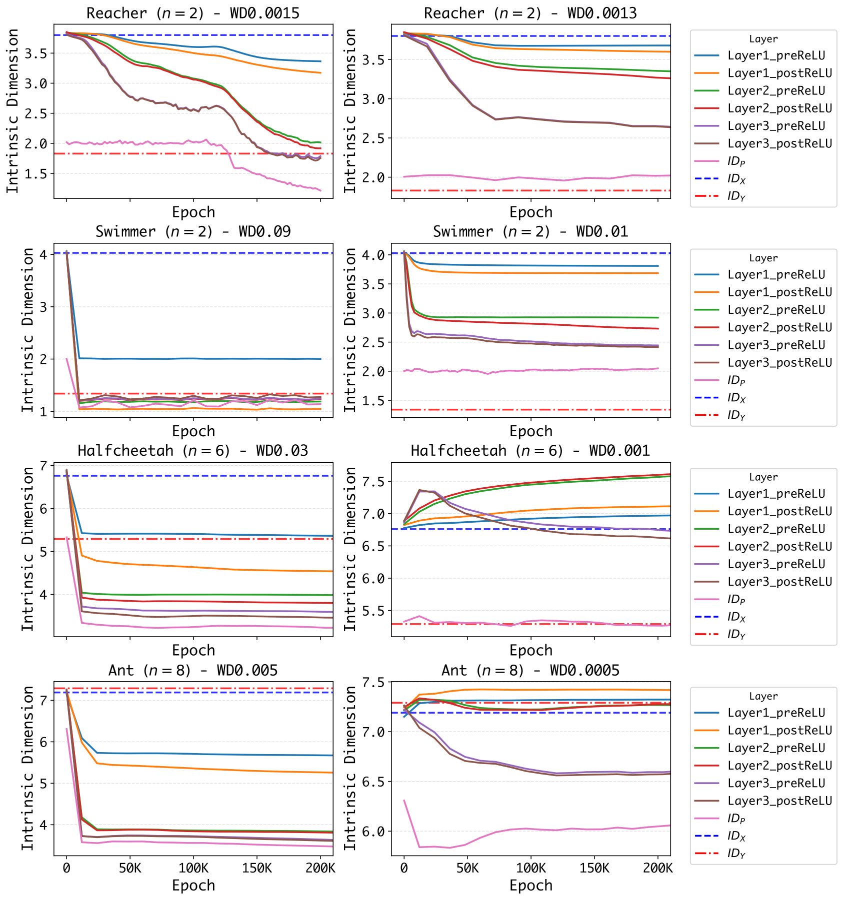

Figure 6: Intrinsic dimension of input, output, and hidden layers over training epochs for a collapsed (left) and a non-collapsed model (right) for MuJoCo datasets. Each subfigure shows the evolution of intrinsic dimension across layers with blue, red dashed, and pink lines denoting the intrinsic dimension of inputs, targets, and predicted outputs, respectively.

E INTRINSIC DIMENSION AND OUTPUT LAYER

We consider here the intrinsic dimension of the outputs (equivalently, the final predictions), ID_P. We will see that here too the relationship between intrinsic dimension and generalization exhibits key differences between classification and regression.

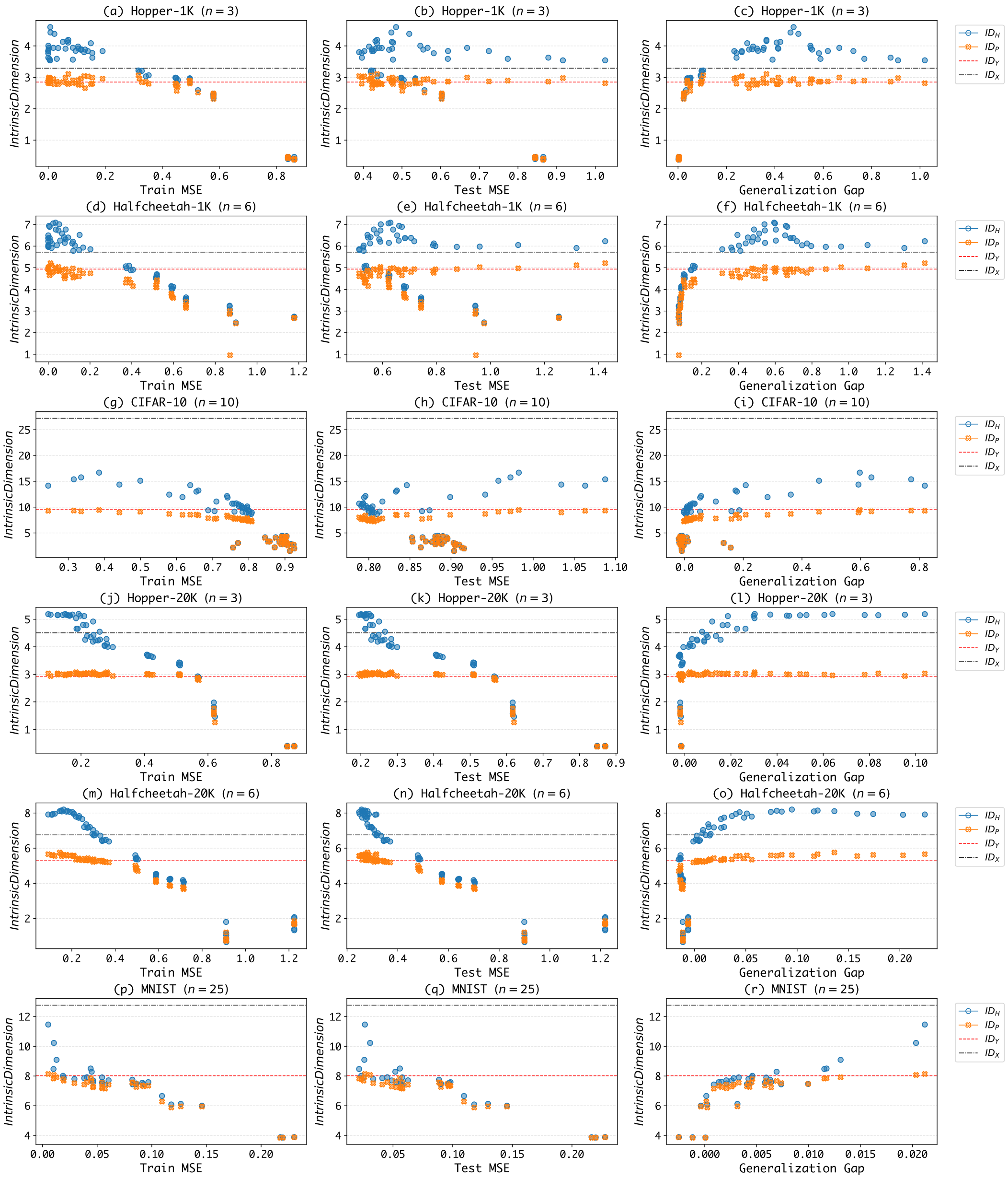

Figure 7: Comparison between ID_H and ID_P for Halfcheetah, Hopper, CIFAR-10, and MNIST datasets

With respect to the output layer, a structural constraint arises from the classification setting. Specifically, the intrinsic dimension of the output layer necessarily satisfies

$$\log_2 C \leq ID_P \leq C,$$

where C is the number of classes. Empirical results consistently show ID_P equals the lower bound of this inequality if the model generalizes well. We refer the reader to the discussion in Section 3.1 of Ansuini et al. (2019). Conversely, saturation of the upper bound, i.e., $ID_P \simeq C$, is associated with poor generalization performance, suggesting that maximal output layer dimensionality corresponds to overfitting in classification tasks, see Section 3.5 in Ansuini et al. (2019).

In contrast, for neural multivariate regression, the structure of the output leads to the trivial bound

$$1 \leq ID_P \leq n,$$

where n is the number of output variates. Interestingly, our empirical findings reveal a departure from the classification setting. As shown in the middle column in Figures 7-8, when the test MSE is low, the intrinsic dimension of the output layer, ID_P satisfies $ID_P \simeq ID_Y$, which can be close to n, saturating the upper bound of the inequality above. Notably, unlike in classification, this saturation is associated with improved test performance. By contrast, when ID_P falls below ID_Y, test MSE performance deteriorates, see Figures 7-8.

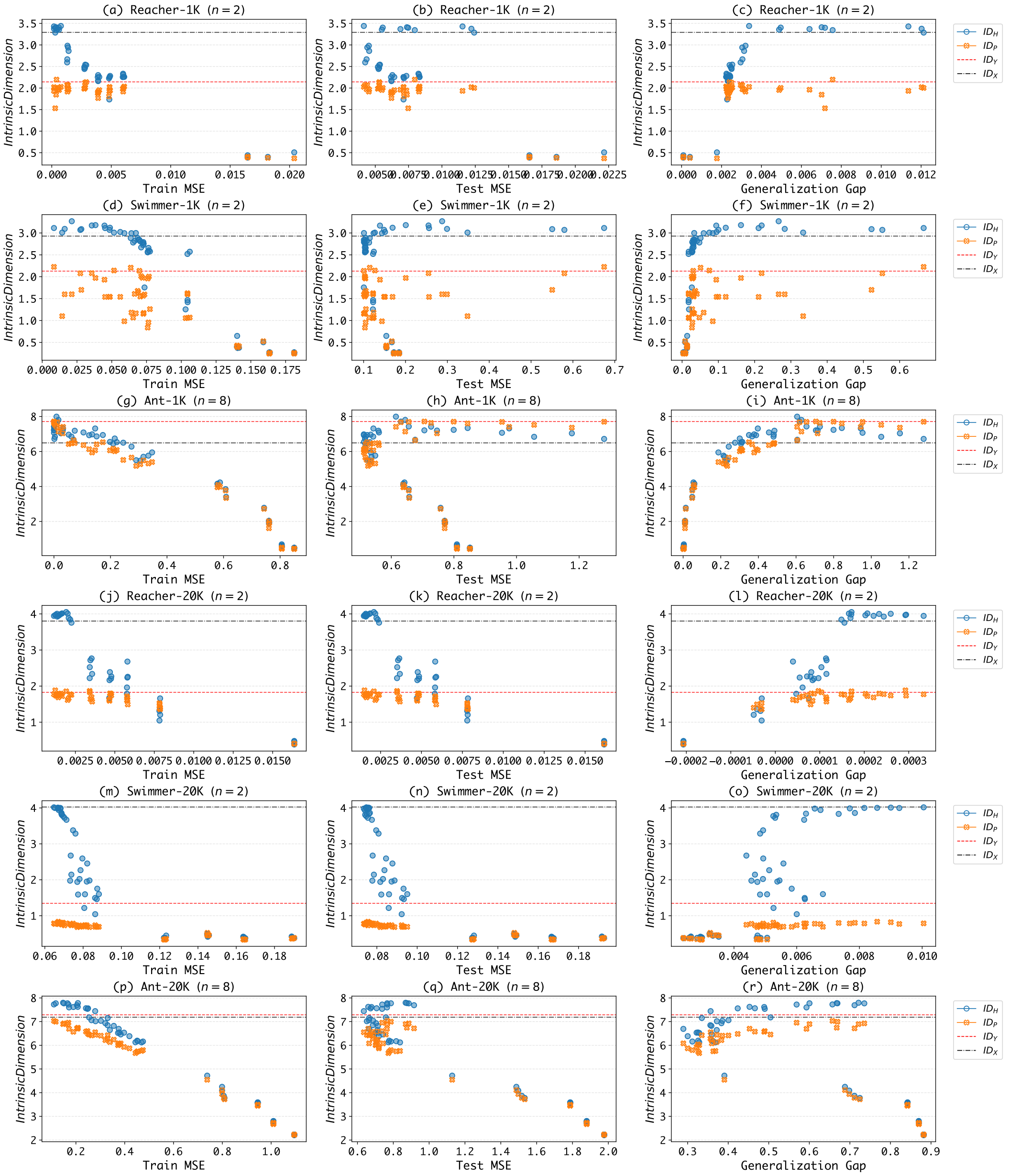

Figure 8: Comparison between ID_H and ID_P for Reacher, Swimmer and Ant datasets

F ADDITIONAL EXPERIMENTS ON GENERALIZATION

This section lists additional results that complement the experiments in the main body for all considered datasets. Figure 9 and 10 shows how generalization power correlates with ID_H. Our key takeaways are summarized in Table 4.

Table 4: Key Takeaways for Generalization.

Regime	ID	Typical behavior
Over-compressed	$\text{ID}_H < \text{ID}_Y$	Underfitting with large train and test MSE
Balanced	$\text{ID}_H \approx \text{ID}_Y$	Sweet spot in low-data and noisy tasks
Under-compressed	$\text{ID}_H \gg \text{ID}_Y$	Benign overfitting with enough low-noise data

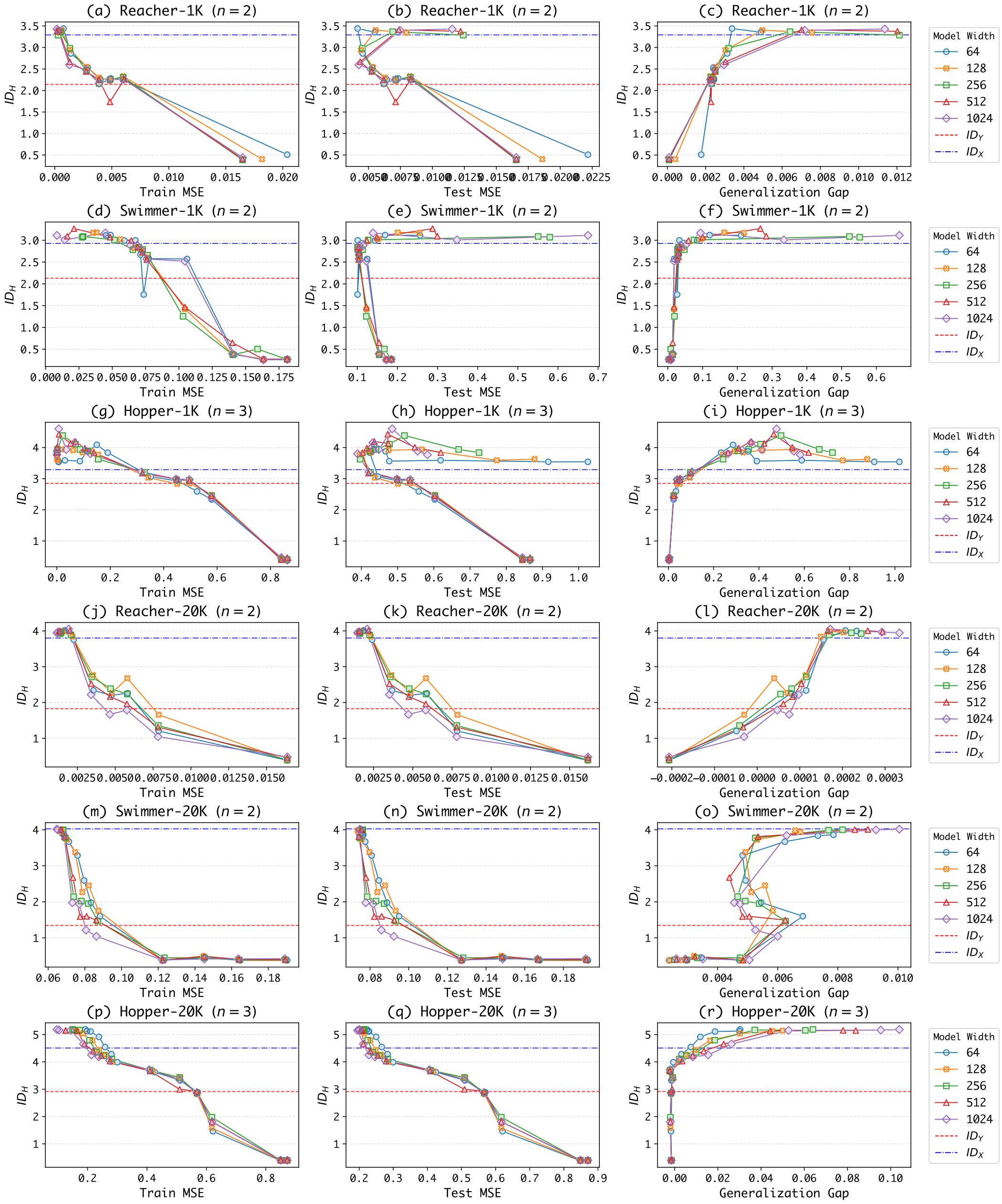

Figure 9: Generalization ability and Intrinsic Dimension for Reacher, Swimmer, and Hopper datasets.

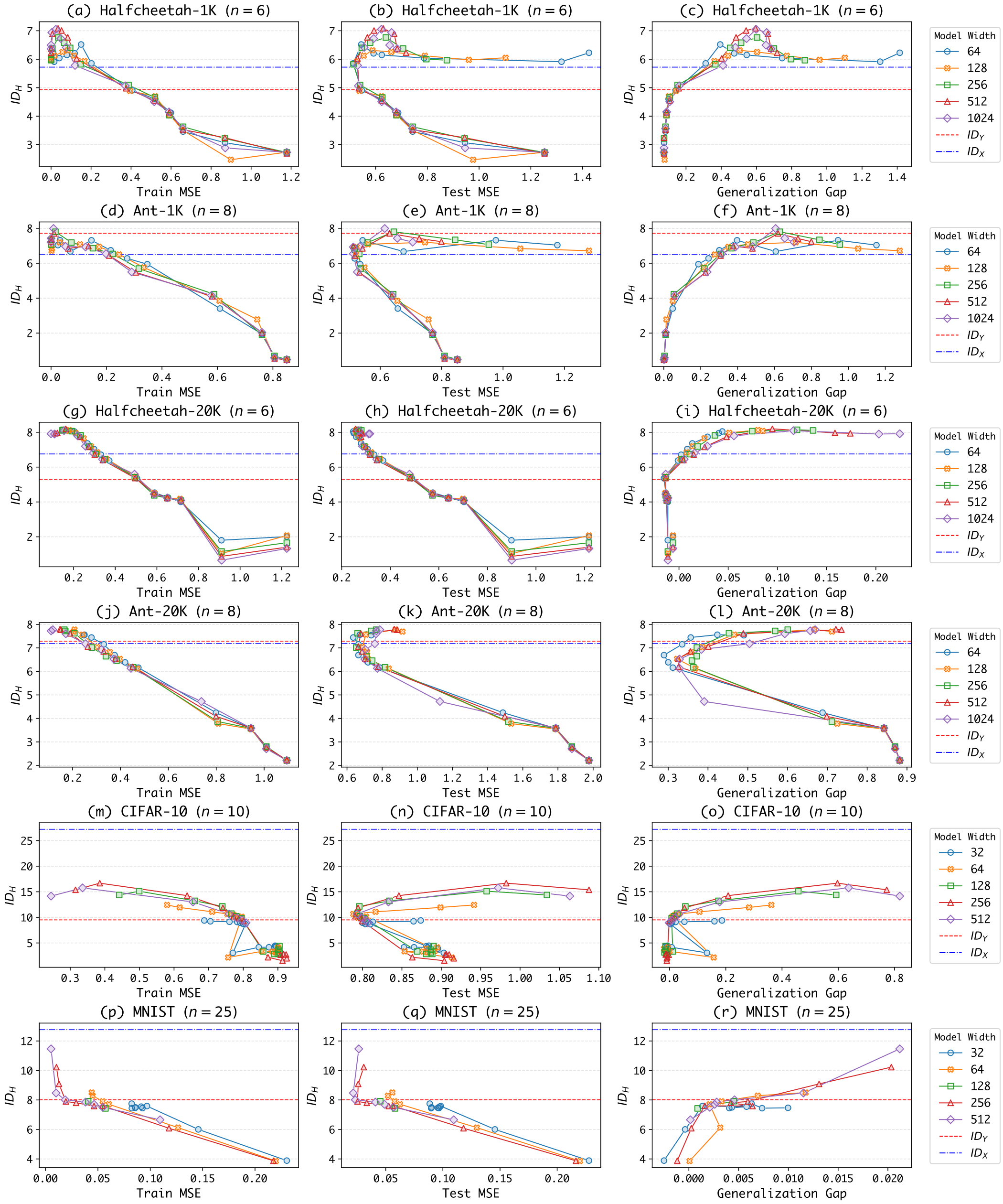

Figure 10: Generalization ability and Intrinsic Dimension for Halfcheetah, Ant, CIFAR-10, and MNIST datasets.

G HOW DOES REGULARIZATION AFFECT NRC AND INTRINSIC DIMENSION?

G.1 WEIGHT DECAY

Weight decay is a canonical and widely adopted model regularization technique for preventing large models from overfitting to data. Real-world applications include but are not limited to (1) regularizing transformer backbones for large language models (Wolf et al., 2020) and robotic generalist policies (Chen et al., 2021); (2) participating, by default, in the common Pytorch implementation of AdamW optimizer (Loshchilov & Hutter, 2019; PyTorch Contributors, 2025) with `weight_decay=0.01`; (3) improving sample efficiency of online reinforcement learning algorithms (Liu et al., 2021; Li et al., 2023b); (4) and facilitating research in model plasticity in deep learning (Lyle et al., 2023; Nauman et al., 2024a; Ceron et al., 2024a).

Figure 11 investigates NRC1 for values of the weight decay parameter λ_{WD}. We see that when λ_{WD} is zero or small, there is no neural regression collapse; but if we increase the weight decay, the NRC1 geometric structure quickly emerges during training. This matches the empirical observation in Andriopoulos et al. (2024).

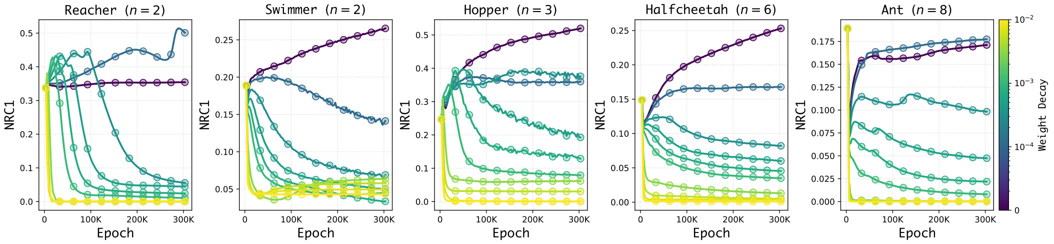

Figure 11: NRC1 decreases as weight decay becomes stronger, leading to model collapse.

G.2 DROPOUT REGULARIZATION

Modern implementations, across deep learning domains, continue to rely on dropout regularization (Srivastava et al., 2014) to mitigate overfitting, underscoring its persistent role in practical training, such as computer vision (Dosovitskiy et al., 2021), NLP (Devlin et al., 2019; Wolf et al., 2020), and reinforcement learning (Hiraoka et al., 2022). We empirically analyze how dropout regularization influences neural regression collapse by varying its strength from a large range ($\in \{0, 0.0001, 0.0005, 0.001, 0.005, 0.01, 0.05, 0.1, 0.2, 0.3, 0.4, 0.5, 0.6, 0.7, 0.8\}$). *No* weight decay is applied. In this section, datasets include Hopper, Halfcheetah, and Ant with two sizes, 1K (Figure 12) and 20K (Figure 13). The horizontal red dashed line represents ID_Y.

Figure 12(a) and Figure 13(a) show the relationship between ID_H and NRC1. We first confirm the same conclusion as made in Section 5, despite the new regularization. ID_H provides a more refined geometric structure than NRC1. Collapsed models with near-zero NRC1 values have varying ID_H below or in the vicinity of $ID_Y < n$, while non-collapsed models with non-trivial NRC1 maintain their ID_H to be above ID_Y and to be positively correlated with $NRC1$. Interestingly, dropout regularization differs from weight decay in that mild dropout (e.g., ≤ 0.01) can effectively prevent models from collapse by increasing both NRC1 and ID_H. This observation sheds light on a geometric interpretation of the effectiveness of mild dropout in reinforcement learning as proposed by Hiraoka et al. (2022).

Figure 12(b) and Figure 13(b) show the relationship between ID_H and test MSE. The results again verify the three regimes discussed in Section 6. For both data sizes, models over-compress features when $ID_H < ID_Y$ and thus lead to increasing test MSE (and thus poor generalization). Then, for small datasets with 1K samples, $ID_H \approx ID_Y$ identifies the sweet spot where test MSE tends to be the lowest and exhibits the ‘U-shape’ plots. Note that models trained with Hopper datasets have not collapsed yet, so they only exhibit the upper part of the ‘U-shape’. Finally, with more samples, e.g., 20K, $ID_H \gg ID_Y$ achieves the best generalization with under-compressed models.

In summary, dropout regularization offers an alternative approach to adjusting the degree of model collapse, while all conclusions drawn from the main body remain intact and inclusive. In addition, mild dropout regularization is more effective than weight decay regularization in increasing NRC1 and ID_H metrics for the under-compressed regime.

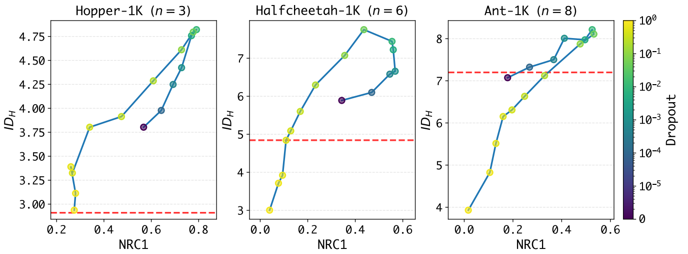

(a) NRC1 - ID_H

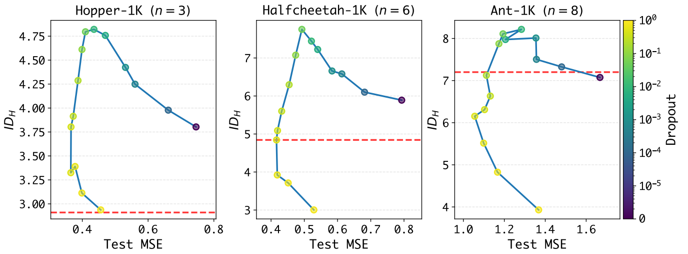

(b) Test MSE - ID_H

Figure 12: Relationship between ID_H and NRC1 and Test MSE for Hopper-1K, Halfcheetah-1K, and Ant-1K datasets, when applying model dropout regularization. The horizontal red dashed line represents ID_Y.

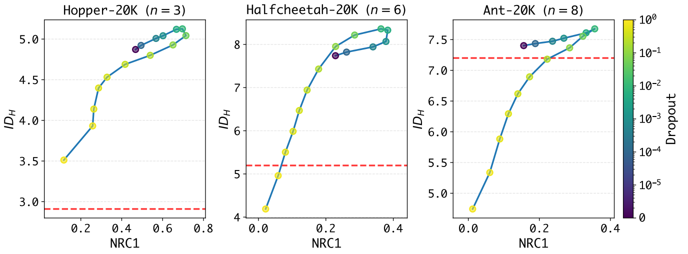

(a) NRC1 - ID_H

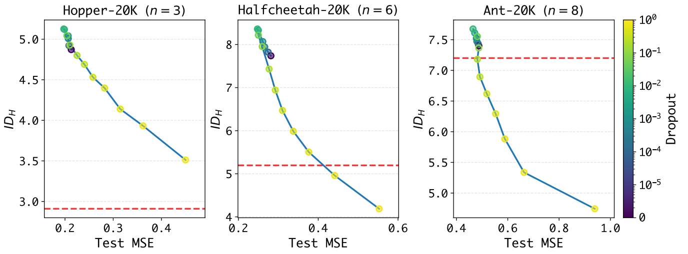

(b) Test MSE - ID_H

Figure 13: Varying model dropout regularization, relationship between ID_H and NRC1 and Test MSE for Hopper-20K, Halfcheetah-20K, and Ant-20K datasets. The horizontal red dashed line represents ID_Y.

G.3 MODEL DEPTH

With mild weight decay regularization, we find that increasing model depth leads to smaller NRC1 and ID_H and thus to more collapsed features. In Figure 14, we examine the relationship between ID_H and NRC1 for Hopper-20K and Halfcheetah-20K datasets. We fix the model width to be 256 and vary the model depth ($\in \{2, 3, 4, 5\}$). For each model depth, we show five mild weight decay values: 0.0001, 0.0003, 0.0005, 0.0007, 0.001. The figure shows that increasing model depth gradually pushes points to the region on the bottom left, where both NRC1 and ID_H are small. For example, Halfcheetah-20K with a depth of 5 can result in collapsed models with $ID_H < ID_Y$.

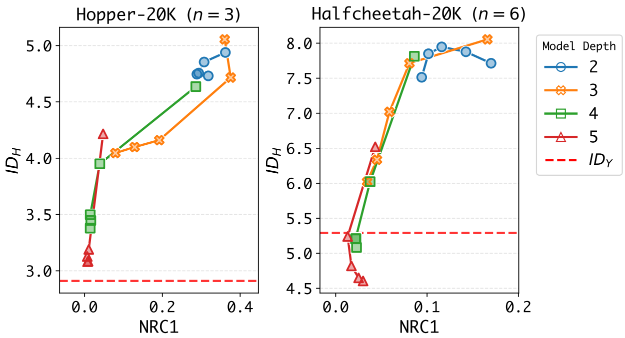

Figure 14: Relationship between ID_H and NRC1 for Hopper-20K and Halfcheetah-20K datasets, when varying model depth. All models have a hidden size of 256. The horizontal red dashed line represents ID_Y.

H EMPIRICAL ANALYSIS ON MORE CHALLENGING TASKS

We extend our empirical analysis to more challenging tasks with varying data sizes, increased intrinsic dimensions, and visual inputs.

Table 5: Overview of additional datasets employed in this section.

Dataset	**Data Size**	**Input Type**	**Input Dim** (D)	**Input ID** (ID_X)	**Target Dim** (n)	**Target ID** (ID_Y)
Humanoid	500,000	raw state	348	11.02	17	9.85
Relocate	500,000	raw state	39	6.90	30	19.82
Cheetah_run	80,000	RGB image	$84 \times 84 \times 9$[3]	8.26	6	6.00
Humanoid_walk	100,000	RGB image	$84 \times 84 \times 9$	9.41	21	14.84

Humanoid (MuJoCo locomotion) The Humanoid dataset (Younis et al., 2024) is generated from the MuJoCo physics simulator, introduced in the main body and Appendix A.1. Each state consists of high-dimensional proprioceptive information, and the corresponding targets are the expert control torques applied at each joint. The goal is to enable the humanoid to run forward stably while maintaining balance, which is substantially more difficult than all previously considered MuJoCo tasks due to its high degrees of freedom and complex contact dynamics. Among all MuJoCo environments, Humanoid is widely regarded as the most challenging.

Relocate (Adroit manipulation) The Relocate dataset (Fu et al., 2020) comes from the Adroit suite (Rajeswaran et al., 2018) of dexterous manipulation tasks. Adroit uses a simulated 24 degrees of freedom (24-DoF) robotic hand, combined with an arm of up to 6-DoF, with rich contact and articulation dynamics. In the Relocate task, the state includes joint positions, velocities, hand pose information, and kinematic information about the ball and target. The action corresponds to the joint torques for the 24 actuators and to the arm movement. The objective is to grasp a small object and

---

[3] Frame stack is commonly applied for visual control tasks. A single observation is of shape $84 \times 84 \times 3$. A frame stack of 3 is used in our experiments, resulting in visual inputs of dimension $84 \times 84 \times 9$.

relocate it to a specified target position. It is a long-horizon manipulation task requiring precise coordination and contact control. Among the four Adroit tasks in the D4RL benchmark (Fu et al., 2020), Relocate is widely considered the most difficult due to its combination of dexterity, precision, and exploration complexity.

Cheetah_run & Humanoid_walk (Visual continuous control) The Cheetah_run and Humanoid_walk datasets (Lu et al., 2023) are visual control benchmarks constructed from demonstrations generated in the DeepMind Control Suite (Tassa et al., 2018). Inputs consist of raw image observations (e.g., 84×84x3 RGB frames), and targets correspond to the continuous control commands. In this section, the Cheetah_run dataset consists of expert demonstrations, as is the case for all previous datasets, while the Humanoid_run dataset contains some noisy suboptimal behavior in addition to the expert demonstrations ('medium-expert dataset'). This adds difficulty in extracting a good policy by imitating the dataset's behavior. We use a CNN image encoder (consisting of 4 `conv2d` layers and ReLU activation), followed by a 3-layer MLP policy network.

Visual control is particularly interesting and challenging because each frame provides only partial information about the system state, effectively forming a Partially Observed Markov Decision Process (POMDP) (Yarats et al., 2022). As a result, the model must infer underlying transition dynamics and identify salient visual features directly from high-dimensional pixel inputs. Within the visual D4RL tasks (Lu et al., 2023), Humanoid_walk is the most challenging due to the humanoid's instability and high-dimensional dynamics, whereas Cheetah_run is comparatively easier but still nontrivial.

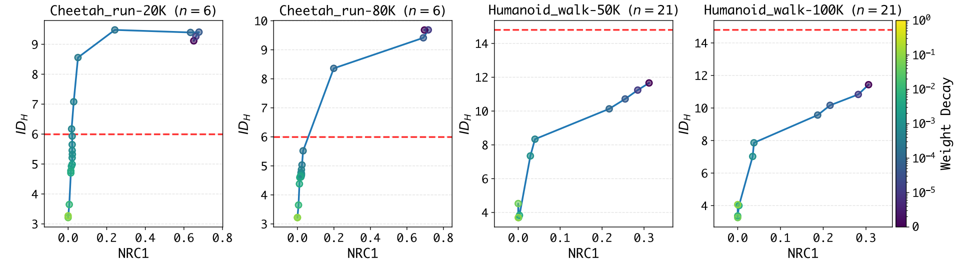

(a) NRC1 - ID_H

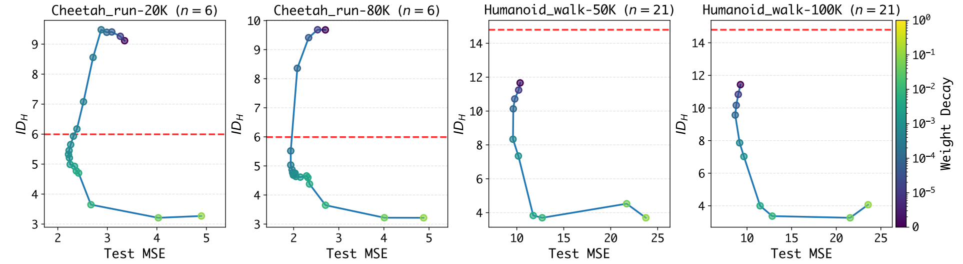

(b) Test MSE - ID_H

Figure 15: Relationship between ID_H and NRC1 and Test MSE for Cheetah_run-20K, Cheetah_run-80K, Humanoid_walk-50K and Humanoid_walk-100K. The horizontal red dashed line represents ID_Y.

H.1 VISUAL CONTROL TASKS

Figure 15(a) shows the relationship between ID_H and NRC1 for the visual control datasets with varying sizes. Consistent with the conclusions in Section 5, ID_H provides a more refined geometric structure than NRC1. Collapsed models with small NRC1 values have varying ID_H below or in the vicinity of $ID_Y < n$, while non-collapsed models with non-trivial NRC1 maintain their ID_H to be above ID_Y and to be positively correlated with NRC1. Notably, for the most challenging Humanoid_walk task, which has a substantially higher ID_Y due to its complex high-dimensional dynamics, models trained with *zero* weight decay initially exhibit neural regression collapse with $ID_H < ID_Y$. This explains the extremely large test MSE observed for Humanoid_walk in Figure 15(b) and its negative correlation with ID_H, which matches the over-compressed regime ($ID_H < ID_Y$) summarized in Table 4. In comparison, the two Cheetah_run datasets exhibit the ‘U-shape’ in the relationship between ID_H and test MSE. This emphasizes the sweet spot with $ID_H \approx ID_Y$, which approaches the lowest test MSE in noisy and challenging tasks.

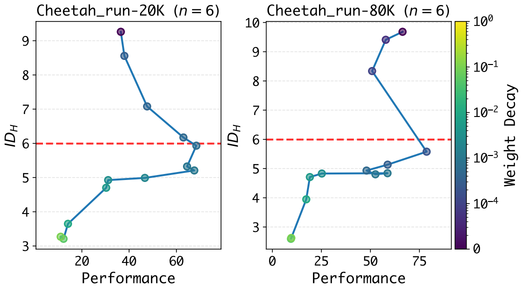

Figure 16: Relationship between ID_H and normalized model performance ($\in [0, 100]$; the higher, the better) by training via behavior cloning on Cheetah_run-20K, and Cheetah_run-80K datasets. We evaluate the trained models to execute locomotion tasks in the DeepMind Control Suite (DMC) robotic simulation (Tassa et al., 2018). The horizontal red dashed line represents ID_Y.

Practical guideline in control tasks Our empirical results have direct implications for evaluating real-world control models, where evaluation is often expensive, unsafe, and risky (Levine et al., 2020). Validation MSE provides little indication of actual control performance in the real tasks. Practitioners must therefore rely on costly real-environment interactions to tune hyperparameters and assess the policy. In Figure 16, we show that the relationship between ID_H and ID_Y not only predicts test MSE but also aligns with the *true* control performance obtained from environment interaction. In particular, the relationship between ID_H and normalized model performance exhibits the opposite ‘U-shape’ behavior, achieving its best score when $ID_H \approx ID_Y$, mirroring the sweet-spot identified in Section 6.

In this way, intrinsic dimension provides a lightweight surrogate for policy evaluation, reducing reliance on frequent, costly, and potentially unsafe real-environment testing. During training, one can monitor the relationship between ID_H and ID_Y to narrow down the hyperparameter search by avoiding the $ID_H < ID_Y$ scenario. When $ID_H \geq ID_Y$, the correlation between ID_H and the test MSE can also reflect its correlation with the real performance.

H.2 RELOCATE & HUMANOID

Humanoid In Figure 17, we show ‘NRC1 - ID_H’ and ‘Test MSE - ID_H’ plots for Humanoid datasets with varying sizes. In Figure 17(a), we observe that ID_H provides a more refined geometric structure than NRC1. Collapsed models with near-zero NRC1 values have varying ID_H below or in the vicinity of $ID_Y < n$, while non-collapsed models with non-trivial NRC1 maintain their ID_H to be above ID_Y and to be positively correlated with NRC1. Then, Figure 17(b) again verifies the three regimes discussed in Section 6. For all data sizes, models over-compress features when $ID_H < ID_Y$ and thus lead to increasing test MSE (and thus poor generalization). Then, for small datasets with 1-50K samples, $ID_H \approx ID_Y$ identifies the sweet spot where test MSE tends to be the lowest and exhibits the ‘U-shape’ plots. Finally, with more samples, e.g., 100-500K, $ID_H > ID_Y$ achieves the best generalization with under-compressed models.

Relocate For the Relocate task with varying data sizes, which have the highest ID_Y due to its complex task dynamics, models trained with *zero* weight decay initially exhibit a severe collapse with both NRC1 ≈ 0 and $ID_H \ll ID_Y$. Unsurprisingly, Test MSE remains large for all data sizes and decay values, and it also negatively correlates with ID_H, uncovering the over-compressed regime.

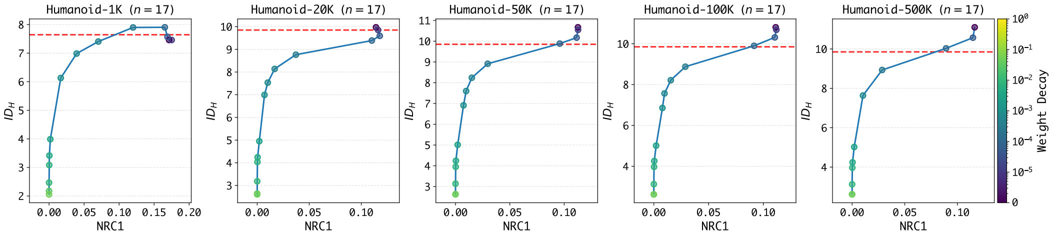

(a) NRC1 - ID_H

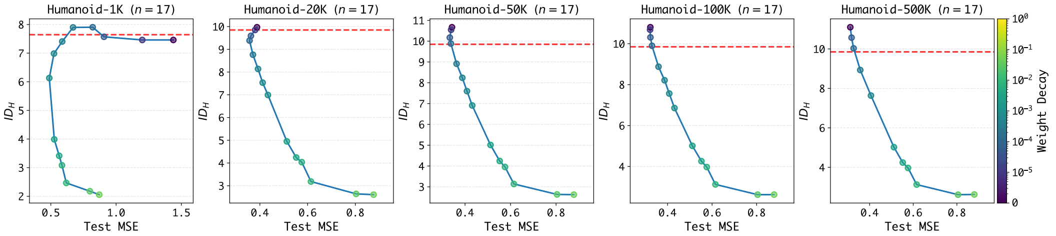

(b) Test MSE - ID_H

Figure 17: Relationship between ID_H and NRC1 and Test MSE, for Humanoid locomotion task, when varying data size ($\in \{1\text{K}, 20\text{K}, 50\text{K}, 100\text{K}, 500\text{K}\}$). The red dashed line represents ID_Y.

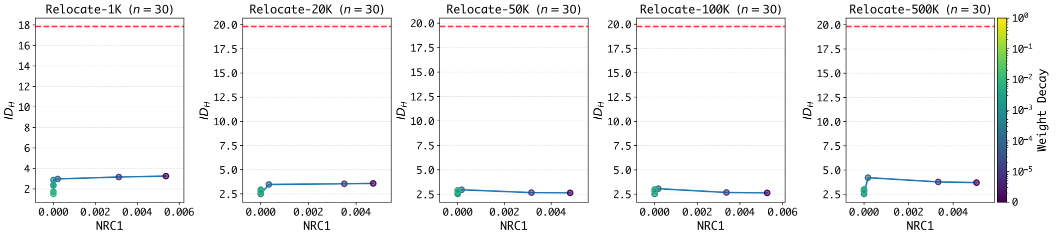

(a) NRC1 - ID_H

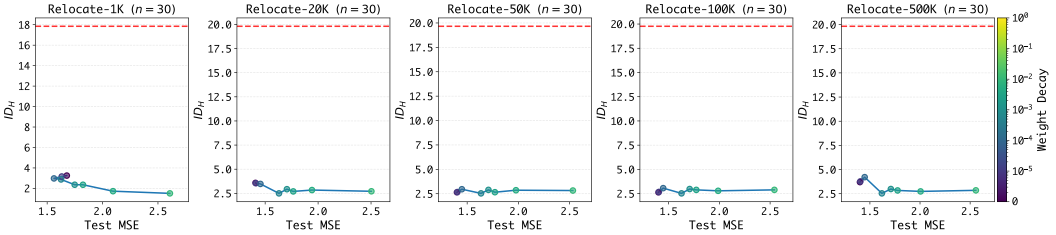

(b) Test MSE - ID_H

Figure 18: Relationship between ID_H and NRC1 and Test MSE, for Relocate manipulation task, when varying data size ($\in \{1\text{K}, 20\text{K}, 50\text{K}, 100\text{K}, 500\text{K}\}$). The red dashed line represents ID_Y.

I MATHEMATICAL ANALYSIS OF REGRESSION COLLAPSE

To provide a principled explanation for the empirical phenomena observed in Section 4, we present a theoretical characterization of regression collapse. We first describe how weight decay induces a dimensional reduction in the feature space and subsequently formalize why this necessitates a reconstruction error.

Why Weight Decay Causes Collapse? We analyze the effect of regularization through the Unconstrained Feature Model (UFM) framework employed in prior work on neural regression collapse (Andriopoulos et al., 2024), where $\lambda_{\mathbf{W}}$ and $\lambda_{\mathbf{H}}$ denote the penalties applied to the weights and features, respectively. By Theorem I.6 established in Appendix I.2, in the limit as $(\lambda_{\mathbf{W}}, \lambda_{\mathbf{H}}) \to 0^+$, the learned features $\mathbf{H}_\lambda$ converge to the minimum-norm solution of the unregularized problem. This solution lies entirely within an n-dimensional subspace, effectively eliminating the $(d-n)$-dimensional null space component of the features. As weight decay increases and starts violating the conditions for affine congruency discussed in Remark I.7, the model enters the over-compressed regime where $ID_H < ID_Y$.

Why Collapsed Models Fail to Generalize? The over-compression creates an unavoidable reconstruction error, which can be formalized by treating the final layer as a smooth map g from the feature manifold to the target space.

Theorem I.1 (Non-surjectivity of Over-compressed Maps)**.** *Let $\mathcal{M}_H$ be a smooth m-dimensional feature manifold and $\mathcal{N}_Y$ be a smooth n-dimensional target manifold, with $m < n$. A smooth map $g : \mathcal{M}_H \to \mathcal{N}_Y$ cannot be surjective; specifically, the image $g(\mathcal{M}_H)$ has Lebesgue measure zero in $\mathcal{N}_Y$.*

As proven in Appendix I.1 via Sard's Theorem, the condition $m < n$ in the over-compressed regime implies that the set of all possible model predictions is a proper subset of the target manifold. Geometrically, there will always be points on the target manifold that lie outside the model's predictive reach, rendering perfect reconstruction mathematically impossible. This explains why over-compressed models consistently correlate with high test MSE, as seen in Figure 4.

I.1 WHY COLLAPSED MODELS FAIL TO GENERALIZE?

The proof of Theorem follows directly from Sard's theorem.

Theorem I.2. *Let $\mathcal{M}$ be a smooth m-dimensional manifold and $\mathcal{N}$ be a smooth n-dimensional manifold, with $m < n$. A smooth map $g : \mathcal{M} \to \mathcal{N}$ cannot be surjective, i.e., $g(\mathcal{M}) \neq \mathcal{N}$.*

Proof. Let $g : \mathcal{M} \to \mathcal{N}$ be a smooth map where $\dim(\mathcal{M}) = m$ and $\dim(\mathcal{N}) = n$, under the condition $m < n$. Consider an arbitrary point $p \in \mathcal{M}$. The differential of the map at this point, $dg_p : T_p\mathcal{M} \to T_{g(p)}\mathcal{N}$, is a linear transformation from the m-dimensional tangent space of $\mathcal{M}$ at p to the n-dimensional tangent space of $\mathcal{N}$ at $g(p)$.

By the rank-nullity theorem, the rank of dg_p is bounded by the dimension of its domain, so it holds that $\text{rank}(dg_p) \leq m$. Given that $m < n$, it follows that $\text{rank}(dg_p) < n$. A linear map is surjective if and only if its rank equals the dimension of its codomain; thus, dg_p is not surjective.

As the choice of p was arbitrary, this holds for all $p \in \mathcal{M}$. By definition, a point is critical if its differential is not surjective. Therefore, every point in the domain $\mathcal{M}$ is a critical point of g. The image of the set of critical points is the set of critical values. In this case, the set of critical values is the entire image of the map, $g(\mathcal{M})$.

By Sard's Theorem, the set of critical values of a smooth map has Lebesgue measure zero in the codomain. It follows that the image $g(\mathcal{M})$ has measure zero in $\mathcal{N}$. However, a smooth n-dimensional manifold (for $n \geq 1$) has positive Lebesgue measure. Since a set of measure zero cannot be equal to a set of positive measure, it must be that $g(\mathcal{M}) \neq \mathcal{N}$.

Therefore, the map g is not surjective. □

This theorem provides the geometric foundation for understanding the failure of collapsed models. In our regression context, the learned features $\{\mathbf{h}_\theta(\mathbf{x})\}$ form a feature manifold $\mathcal{M}_H$ of dimension

$m = ID_H$, while the targets $\{\mathbf{y}\}$ lie on a target manifold $\mathcal{N}_Y$ of dimension $n = ID_Y$. The final layer of the network constitutes a smooth map from the feature manifold to the target space.

When a model is in the over-compressed regime ($ID_H < ID_Y$), the theorem's condition ($m < n$) is met. The direct consequence is that this smooth map cannot be surjective. This means the image of the feature manifold—the set of all possible predictions the model can generate—is a proper subset of the target manifold. Geometrically, there will always be points on the target manifold that lie outside the model's predictive reach. A perfect reconstruction is therefore impossible, as the model is fundamentally incapable of generating the full range of target data, leading to an unavoidable error.

I.2 WHY WEIGHT DECAY LEADS TO COLLAPSE: ANALYSIS VIA THE UNCONSTRAINED FEATURE MODEL

In this section, we provide a theoretical explanation for why weight decay causes neural regression collapse through the lens of the Unconstrained Feature Model (UFM). The UFM is a simplified mathematical abstraction that does not capture all aspects of practical neural networks, but provides insight into the geometric mechanisms by which regularization constrains learned representations.

The UFM abstracts the neural regression problem by treating the feature extractor $h_\theta(\cdot)$ as producing arbitrary feature vectors $\mathbf{h}_i \in \mathbb{R}^d$ for each input $\mathbf{x}_i$, collected into a feature matrix $H \in \mathbb{R}^{d\times M}$. The final prediction is obtained via a linear map $W \in \mathbb{R}^{n\times d}$ and bias $\mathbf{b} \in \mathbb{R}^n$, giving predictions $\hat{Y} = WH + \mathbf{b}\mathbf{1}^\top$. The UFM objective is:

$$\min_{W,H,\mathbf{b}} \frac{1}{2M}\|WH + \mathbf{b}\mathbf{1}^\top - Y\|_F^2 + \frac{\lambda_W}{2}\|W\|_F^2 + \frac{\lambda_H}{2}\|H\|_F^2 \tag{1}$$

The model is "unconstrained" because H can be any matrix in $\mathbb{R}^{d\times M}$, unlike in actual neural networks, where H is constrained by the input data and network architecture. In the UFM, we typically have $d \gg n$, mirroring the overparameterized regime where feature dimension greatly exceeds target dimension.

The optimal bias is $\mathbf{b}^* = \bar{\mathbf{y}}$ where $\bar{\mathbf{y}} = \frac{1}{M}\sum_{i=1}^{M}\mathbf{y}_i$. Defining the centered target matrix $\tilde{Y} = Y - \bar{\mathbf{y}}\mathbf{1}^\top \in \mathbb{R}^{n\times M}$, the problem reduces to:

$$\min_{W,H} \frac{1}{2M}\|WH - \tilde{Y}\|_F^2 + \frac{\lambda_W}{2}\|W\|_F^2 + \frac{\lambda_H}{2}\|H\|_F^2 \tag{2}$$

We denote the empirical covariance by $\Sigma = \frac{1}{M}\tilde{Y}\tilde{Y}^\top \in \mathbb{R}^{n\times n}$, and assume Σ is full rank with eigenvalues $\lambda_1 \geq \lambda_2 \geq \cdots \geq \lambda_n > 0$. A key quantity is $c = \lambda_W\lambda_H$.

We first restate the characterization of global minimizers when regularization is present, adapted from Theorem 4.1 of Andriopoulos et al. (2024). We focus on the regime where $c < \lambda_n$ since we are interested in the limiting behavior when $\lambda_H \to 0$ and $\lambda_W \to 0$.

Theorem I.3 (Regularized UFM Solution, adapted from Andriopoulos et al. (2024)). *Suppose $0 < c < \lambda_n$. Define $A = \Sigma^{1/2} - \sqrt{c}I_n$. Then any global minimizer (W_λ, H_λ) of equation 2 can be expressed as:*

$$W_\lambda = \left(\frac{\lambda_H}{\lambda_W}\right)^{1/4} A^{1/2}R \tag{3}$$

$$H_\lambda = \left(\frac{\lambda_W}{\lambda_H}\right)^{1/4} R^\top A^{1/2}(\Sigma^{1/2})^{-1}\tilde{Y} \tag{4}$$

where $R \in \mathbb{R}^{n\times d}$ is any matrix satisfying $RR^\top = I_n$.

Proof. This follows from Theorem 4.1 of Andriopoulos et al. (2024) with $c < \lambda_n$ implying $j^* = n$. □

The regularized solution has a specific dimensional structure. Since $A^{1/2}(\Sigma^{1/2})^{-1}\tilde{Y} \in \mathbb{R}^{n\times M}$ and $R^\top \in \mathbb{R}^{d\times n}$, the matrix $H_\lambda \in \mathbb{R}^{d\times M}$ has columns lying in the column space of $R^\top$, which is at most

n-dimensional. Even though H_λ lives in a d-dimensional ambient space with $d \gg n$, its columns are confined to an n-dimensional subspace.

When regularization is absent, the problem has infinitely many global minimizers, characterized by the following theorem from Andriopoulos et al. (2024).

Theorem I.4 (Unregularized UFM Solutions, from Andriopoulos et al. (2024))**.** *When $\lambda_W = \lambda_H = 0$, a pair (W, H) is a global minimizer of equation 2 if and only if $WH = \tilde{Y}$ and W has full row rank. For any such W, the corresponding global minimizers in H are:*

$$H_{\textit{unreg}} = W^\dagger \tilde{Y} + (I_d - W^\dagger W)Z \tag{5}$$

where $W^\dagger$ is the Moore–Penrose pseudoinverse and $Z \in \mathbb{R}^{d\times M}$ is arbitrary.

Proof. See Theorem 4.3 of Andriopoulos et al. (2024). □

The structure in equation 5 decomposes solutions into two orthogonal components: $W^\dagger\tilde{Y}$ lies in the row space of W (dimension at most n), while $(I_d - W^\dagger W)Z$ lies in the null space of W (dimension exactly $d - n$). The Frobenius norm satisfies $\|H_{\text{unreg}}\|_F^2 = \|W^\dagger\tilde{Y}\|_F^2 + \|(I_d - W^\dagger W)Z\|_F^2$ by orthogonality. The minimum-norm solution is achieved when $Z = 0$, eliminating the $(d - n)$-dimensional null space component. When $Z \neq 0$, the null space allows H to span up to d dimensions, whereas $Z = 0$ confines H to at most n dimensions.

We now investigate what happens to the regularized solution as weight decay vanishes, examining the limit $\lambda_W, \lambda_H \to 0$ while maintaining $\lambda_H/\lambda_W = k > 0$.

Lemma I.5 (Limiting Reconstruction)**.** *Suppose $\lim_{\lambda_H\to 0,\lambda_W\to 0}(\lambda_H/\lambda_W) = k > 0$ and let (W_λ, H_λ) be as in Theorem I.3. Then:*

$$\lim_{\lambda_W,\lambda_H\to 0} W_\lambda H_\lambda = \tilde{Y} \tag{6}$$

Proof. Since $c = \lambda_W\lambda_H \to 0$, Theorem I.3 applies for sufficiently small λ_W, λ_H. Multiplying:

$$W_\lambda H_\lambda = \left(\frac{\lambda_H}{\lambda_W}\right)^{1/4} A^{1/2}R \cdot \left(\frac{\lambda_W}{\lambda_H}\right)^{1/4} R^\top A^{1/2}(\Sigma^{1/2})^{-1}\tilde{Y} \tag{7}$$

$$= A^{1/2}(RR^\top)A^{1/2}(\Sigma^{1/2})^{-1}\tilde{Y} = A(\Sigma^{1/2})^{-1}\tilde{Y} \tag{8}$$

Substituting $A = \Sigma^{1/2} - \sqrt{c}I_n$:

$$W_\lambda H_\lambda = (\Sigma^{1/2} - \sqrt{c}I_n)(\Sigma^{1/2})^{-1}\tilde{Y} = (I_n - \sqrt{c}\Sigma^{-1/2})\tilde{Y} \tag{9}$$

As $c \to 0$, this yields $\tilde{Y}$. □

Theorem I.6 (Limiting Solution Structure)**.** *Under the assumptions of Lemma I.5, define:*

$$W_0 = \lim_{\lambda_W,\lambda_H\to 0} W_\lambda = k^{1/4}\Sigma^{1/4}R \tag{10}$$

$$H_0 = \lim_{\lambda_W,\lambda_H\to 0} H_\lambda = k^{-1/4}R^\top\Sigma^{-1/4}\tilde{Y} \tag{11}$$

Then (W_0, H_0) is a global minimizer of the unregularized problem with:

$$H_0 = W_0^\dagger\tilde{Y} \tag{12}$$

In particular, H_0 has no null space component (i.e., $Z = 0$ in Theorem I.4).

Proof. From Lemma I.5, $W_0H_0 = \tilde{Y}$, so (W_0, H_0) is a global minimizer. Since $W_0 = k^{1/4}\Sigma^{1/4}R$ has full row rank, its pseudoinverse is:

$$W_0^\dagger = W_0^\top(W_0W_0^\top)^{-1} = (k^{1/4}\Sigma^{1/4}R)^\top(k^{1/2}\Sigma^{1/2})^{-1} = k^{-1/4}R^\top\Sigma^{-1/4} \tag{13}$$

Thus $W_0^\dagger\tilde{Y} = k^{-1/4}R^\top\Sigma^{-1/4}\tilde{Y} = H_0$, confirming $Z = 0$. For any H satisfying $W_0H = \tilde{Y}$, we have $H = W_0^\dagger\tilde{Y} + (I_d - W_0^\dagger W_0)Z$ with:

$$\|H\|_F^2 = \|W_0^\dagger\tilde{Y}\|_F^2 + \|(I_d - W_0^\dagger W_0)Z\|_F^2 \geq \|H_0\|_F^2 \tag{14}$$

by orthogonality, with equality if and only if $Z = 0$. Thus H_0 is the minimum-norm solution. □

These results explain why weight decay causes dimensional collapse. Without regularization, H can utilize the full d-dimensional space through the arbitrary null space component $(I_d - W^\dagger W)Z$, where the null space has dimension $d - n$. With any positive regularization, Theorem I.3 shows H_λ is confined to an at most n-dimensional subspace. Theorem I.6 proves that even as $\lambda_W, \lambda_H \to 0^+$, the limiting solution has $Z = 0$, eliminating the $(d - n)$-dimensional null space component. This demonstrates that even infinitesimally small weight decay induces dimensional collapse by biasing toward the minimum-norm solution of the unregularized problem, which lies entirely in the n-dimensional row space of W. Since typically $d \gg n$, this represents a massive dimensional reduction from the ambient feature space to a low-dimensional subspace determined by the target structure.

Remark I.7 (Breakdown of Affine Congruence in the Over-Compressed Regime.). Theorem I.3, adapted from Theorem 4.1 of Andriopoulos et al. (2024), characterizes global minimizers of the regularized UFM objective in terms of the parameter

$$c := \lambda_W \lambda_H$$

and the eigenvalues $\lambda_1 \geq \cdots \geq \lambda_n > 0$ of the target covariance Σ. When $0 < c < \lambda_n$, the theorem yields $j^* = n$, and the solution satisfies

$$H_\lambda = \left(\frac{\lambda_W}{\lambda_H}\right)^{1/4} R^\top A^{1/2} (\Sigma^{1/2})^{-1} \tilde{Y}, \quad A = \Sigma^{1/2} - \sqrt{c}\, I_n,$$

with $A \succ 0$. In this regime, $A^{1/2}$ is full rank and the map relating H_λ and $\tilde{Y}$ is an invertible affine transformation on the support of $\tilde{Y}$. Consequently, the learned features and targets are affine congruent, implying preservation of intrinsic dimension:

$$ID_H = ID_Y.$$

In contrast, when $c \geq \lambda_n$, Theorem 4.1 of Andriopoulos et al. (2024) yields $j^* < n$, and the solution involves truncated matrices $[A^{1/2}]_{j^*}$ and $[\Sigma^{1/2}]_{j^*}$ obtained by retaining only the eigenspaces corresponding to eigenvalues $\lambda_i > c$. In this case, the resulting feature matrix satisfies

$$\text{rank}(H_\lambda) \leq j^* < n,$$

and the affine map relating H_λ and $\tilde{Y}$ is no longer invertible on the support of $\tilde{Y}$. As a consequence, affine congruency is not guaranteed to hold. This regime allows for a reduction in intrinsic dimension,

$$ID_H < ID_Y,$$

which is precisely what we observe empirically in the over-compressed region. This observation highlights the diagnostic value of intrinsic dimension: deviations between ID_H and ID_Y signal departure from the regime in which the assumptions underlying affine congruency hold. Although the parameter c is not directly observable in practice, as it arises from the UFM abstraction rather than explicit training dynamics, intrinsic dimension provides an empirical proxy for this regime. In particular, the transition from $ID_H \approx ID_Y$ to $ID_H < ID_Y$ indicates that the effective regularization has crossed the threshold $c = \lambda_n$, placing the model in the over-compressed regime and violating the conditions under which affine congruency is expected.

J LIMITATIONS AND FUTURE WORK

While our work provides new geometric insights into neural multivariate regression through intrinsic dimension analysis, some limitations remain. Although we provide some theoretical results explaining why weight decay causes collapse (Appendix I.2) and why collapsed models often fail (Appendix I.1), a complete theoretical characterization of the relationship between intrinsic dimension and generalization is not yet available. Additionally, the 2-NN estimator we employ provides reliable estimates for intrinsic dimensions below approximately 20. For extremely high-dimensional target spaces or feature representations, alternative estimation methods may be necessary. Finally, our practical guidelines rely on adjusting standard hyperparameters (weight decay, model depth, dropout) to indirectly control ID_H. A more principled approach would be to optimize ID_H during training; however, the 2-NN estimator is non-differentiable and cannot be optimized via backpropagation.

Several promising directions emerge from our findings. Deriving generalization bounds that incorporate intrinsic dimension would provide a rigorous theoretical foundation for the empirical relationships we observe. Theoretical frameworks beyond the UFM could offer additional perspectives on how network architecture, training dynamics, and regularization jointly determine the intrinsic dimension of learned representations. Differentiable intrinsic dimension estimation remains largely underexplored; developing robust, efficient, and scalable differentiable estimators that enable direct control of ID_H during training via backpropagation represents an important research direction. Such advances would allow practitioners to explicitly target desired intrinsic dimensions rather than adjusting hyperparameters indirectly, and would broaden the applicability of our analysis to higher-dimensional settings. Finally, exploring whether intrinsic dimension provides similar insights for other learning paradigms, such as generative modeling, reinforcement learning, and multi-task learning, could offer a unifying geometric perspective across domains.

K SCIENCE OF DL IMPROVEMENT CHALLENGE SUBMISSION

K.1 WHAT MODEL ARE YOU TARGETING?

Provide a summary of the problem the deep net model is designed to solve. Good summaries should outline the state of the literature, provide an overview that domain experts would consider reasonable, and cite relevant sources.

We study standard model architectures, including multi-layer perceptron (MLP) policies operating on raw states for state-based control tasks; and convolutional neural network (CNN) feature encoders followed by an MLP policy head, for vision-based tasks. Despite their simplicity, these architectures remain the mainstream choice in classic online and offline reinforcement learning (RL) algorithms(Fujimoto et al., 2018; Haarnoja et al., 2018; Emmons et al., 2022; Yarats et al., 2022; Kostrikov et al., 2022; Tarasov et al., 2023; Xu et al., 2024), as naively scaling model size often leads to instability or degraded performance(Ota et al., 2021; Nauman et al., 2024a; Lyle et al., 2024; Ceron et al., 2024b), and more advanced model architectures are still ongoing research questions with less understanding (Nauman et al., 2024b; Lee et al., 2025a;b; Wang et al., 2025).

Recent literature highlights the importance of regularization—such as weight decay(Nauman et al., 2024b), dropout(Hiraoka et al., 2022), and layer normalization(Nauman et al., 2024b; Wang et al., 2025)—to stabilize training, improve generalization, and enable limited scaling in RL settings (Liu et al., 2021; Kumar et al., 2022; Li et al., 2023b). The regularized models studied in this work align with these practices, making our findings potentially applicable to these commonly used RL pipelines.

K.2 HOW DO YOUR RESULTS CONTRIBUTE—OR COULD POTENTIALLY CONTRIBUTE—TO UNDERSTANDING THESE MODELS?

What aspects of the models become better understood thanks to your work?

Visual control is particularly interesting and challenging because each pixel frame provides only partial information about the system state, forming a Partially Observed Markov Decision Process (POMDP) (Yarats et al., 2022). Appendix H.1 experiments with such a vision control task by behavior-cloning an expert demonstration dataset generated from the simulated Cheetah_run environment. We use a 4-layer CNN image encoder, followed by a 3-layer MLP policy to produce actions.

Our empirical results have direct implications for evaluating real-world control models, where evaluation is often expensive, unsafe, and risky (Levine et al., 2020). Validation MSE provides little indication of actual control performance in the real tasks. Practitioners must therefore rely on costly real-environment interactions to tune hyperparameters and assess the policy. Figure 19 shows that the relationship between ID_H and ID_Y not only predicts test MSE but also aligns with the *true* control performance obtained from environment interaction. In particular, the relationship between ID_H and normalized model performance exhibits the opposite ‘U-shape’ behavior, achieving its best score when $ID_H \approx ID_Y$, mirroring the sweet-spot identified in Section 4.

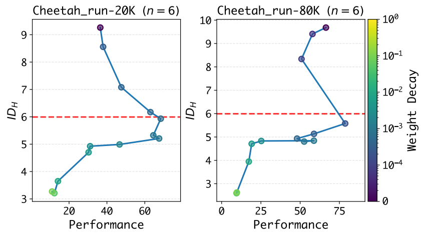

Figure 19: Relationship between ID_H and normalized model performance ($\in [0, 100]$; the higher, the better). The horizontal red dashed line represents ID_Y.

K.3 HOW DO YOU EXPECT YOUR SUBMISSION TO INFLUENCE FUTURE WORK?

Propose ways in which your insights, findings, or methodologies could shape subsequent research directions, model design choices, or scientific applications.

Prior work often associates strong online/offline RL performance with high feature rank of critics and actors (Kumar et al., 2021; Lyle et al., 2022; Nauman et al., 2024a). Our findings suggest an alternative perspective: improved performance may arise from constraining representation geometry such that feature intrinsic dimension matches task-relevant targets, rather than maximizing expressivity. This insight motivates future work on geometry-aware representation learning for RL, potentially grounded in the manifold hypothesis, as done recently by Li & He (2025) and Tiwari et al. (2025).